P. Walter Agostinelli, Davide Laera, Isaac Boxx, Laurent Gicquel, Thierry Poinsot, Impact of wall heat transfer in Large Eddy Simulation of flame dynamics in a swirled combustion chamber, Combustion and Flame 234 (2021) 111728.

The original publication is available at www.elsevier.com

https://doi.org/10.1016/j.combustflame.2021.111728

Impact of wall heat transfer in Large Eddy Simulation of flame dynamics in a swirled combustion chamber

P. W. Agostinelli[a,b,*], D. Laera[b], I. Boxx[c], L. Gicquel[b], T. Poinsot[d]

[a] *Safran Helicopter Engines, 64510 Bordes, France*
[b] *CERFACS, 42 avenue Gaspard Coriolis, 31057 Toulouse, France*
[c] *Institut für Verbrennungstechnik, Deutsches Zentrum für Luft-und Raumfahrt (DLR), Stuttgart, Germany*
[d] *Institut de Mécanique des Fluides de Toulouse, IMFT, Université de Toulouse, CNRS, Toulouse 31400, France*

Abstract

Large Eddy Simulation (LES) is a fundamental research tool to study gas turbines and aero-engine combustors. In LES, although rarely addressed systematically, it is known that thermal boundary conditions control the heat transfer between the flow and the combustor walls. This work presents a study on the impact of thermal wall boundary conditions for the PRECCINSTA test bench, operated by the German Space Agency (DLR). Two approaches are tested: Heat Resistances Tuning (HRT), where a local resistance is tuned using experimental temperature data, and full Conjugate Heat Transfer (CHT), where the chamber wall-temperature is solved and coupled to the flow computation. Results reveal that the HRT method captures the mean flame correctly but the predicted flame becomes unstable and responds to a thermoacoustic oscillation which is not observed experimentally. On the contrary, using CHT, the flame is correctly predicted and stable as in the experiments. Finally, to understand the differences between the HRT and the CHT simulations, Dynamic Mode Decomposition (DMD) analysis is performed showing that the correct response of the flame branches to the pressure oscillations is recovered only in the CHT simulations for which thermoacoustically stable operations are retrieved.

Keywords: Conjugate Heat Transfer; Large Eddy Simulation; Thermoacoustic instabilities; Turbulent flames

*Corresponding author: agostinelli@cerfacs.fr

Nomenclature

Acronyms

ARC	Analytically Reduced Chemistry
CB	Centerbody
CFL	Courant-Friedrichs-Lewy
CHT	Conjugate Heat Transfer
CRZ	Central Recirculation Zone
DMD	Dynamic Mode Decomposition
FFT	Fast Fourier Transform
FTF	Flame Transfer Function
HRT	Heat Resistance Tuning
LES	Large Eddy Simulation
LOS	Line-of-sight
ORZ	Outer Recirculation Zone
OTA	Optically Thin Assumption
PCS	Parallel Coupling Strategy
pdf	Probability density function
PLIF	Planar Laser-Induced Fluorescence
RMS	Root Mean Square
sPIV	Stereoscopic Particle Image Velocimetry
TFLES	Thickened-flame LES
W	Walls

Greek Symbols

β_{Ch}	Charlette coefficient
δt	Time step
$\dot{m}$	Mass flow rate
ϵ	Emissivity
λ	Thermal conductivity
$\mathcal{R}e(\widehat{RI})$	Real part of the Rayleigh index
$\mathcal{T}_{\phi,p}$	Equivalence ratio - pressure fluctuations correlation index
Φ	Equivalence ratio
ϕ	Phase
Φ_q	Heat flux
ρ	Density
σ	Stefan-Boltzmann constant
τ	Characteristic time

Roman Symbols

$\dot{q}$	Heat release rate
$\mathcal{R}$	Reflection coefficient
Bi	Biot number
C	Heat capacity
c	Sound speed
h	Heat transfer coefficient
K	Relaxation coefficient
L	Characteristic length
P	Power
p'	Pressure fluctuation
S	Surface
t	Time
U	Velocity
V	Volume
$y+$	Dimensionless wall distance
R	Thermal resistance
T	Temperature

Subscripts

σ	Root Mean Square
θ	Tangential component
air	Air line
$cond$	Conduction
$conv$	Convection
eq	Equivalent
exp	Experimentally observed
f	Fluid
$fuel$	Fuel line
num	Numerically predicted
r	Radial component
rad	Radiation
ref	Reference
s	Solid

th Thermal

$wall, ext$ External wall

$wall, int$ Internal wall

z Axial component

1. Introduction

Large Eddy Simulation (LES) is a powerful method to investigate flow physics in complex geometries, including swirling reacting flows often present in gas-turbine combustors [1–4] and complex multi-physics phenomena such as the coupling between the flame and acoustics as experienced in thermoacoustic combustion instabilities [5, 6]. Nevertheless, such simulations are often performed with simple boundary conditions on walls, where temperature is either imposed or adiabaticity is assumed, although these thermal boundary conditions control the heat transfer between the flow and the combustor walls [7]. The chemical reactions inside the combustion chamber are furthermore strongly dependent on the temperature field so that wall boundary conditions can affect the flame shape [8], its stabilization [9] to the point where it can even extinguish the flame (e.g. when it interacts with walls [10, 11]). Thermoacoustic instabilities are also highly impacted by temperature boundary conditions: a change in the temperature field modifies the laminar flame speed [12] and the local speed of sound, impacting the frequency of the acoustic resonant modes [13, 14] as well as the response of the flame to acoustic oscillations, usually described by the Flame Transfer Function (FTF) [15].

Multiple experimental and numerical studies have focused on the impact of heat transfer on flame stabilization and dynamics. A detailed experimental analysis of the influence of heat losses on the flame shape was proposed by Guiberti *et al.* [8], who underlined the important role played by the temperature boundary conditions in the flame stabilization. Mejia *et. al* [16] experimentally investigated the impact of the wall-temperature on a laminar flame stabilized on a slot burner. Thermoacoustically stable or unstable configurations have been recorded depending on the temperature of the burner at the flame anchoring point which altered the flame foot dynamics. Indeed, as suggested by Kedia *et. al* [17], flame-wall interaction can be crucial in closing the feedback loop between heat release rate and velocity oscillations. The importance of the temperature field near the flame anchoring region has also been underlined by Hong *et. al* [18], who investigated the dynamic instability characteristics of a turbulent premixed flame in a backward-facing step combustor and showed that the wall thermal conductivity influenced the flame speed near the flame holder, leading to a distinct dynamic behavior of the flame for each flame holder material. For example, replacing the stainless steel flame holder with one made of ceramics inhibited the onset of combustion instability. Similarly, Cuquel *et. al* [19] investigated the effect of unsteady heat losses between the flame base and burner rim on the FTF. Improved expressions for the FTF of conical flames submitted to velocity disturbances were obtained by including a model for the motion of the flame base due to the unsteady heat losses. An important effect of heat transfer has been observed for turbulent flames too. Lohrmann *et. al* [20] investigated the influence of the preheat temperature on the FTF of a turbulent swirl-stabilized premixed flame. By increasing the preheat temperature, the delay of the flame response decreased due to an increase in the turbulent flame speed that shifted the main reaction zone to an upstream location. The influence of the transient combustor wall-temperature on the thermoacoustic oscillations of turbulent premixed flames has been investigated by Heydarlaki *et. al* [21]. They showed that the probability of occurrence of large amplitude oscillations was dependent on the initial wall-temperature, confirming the strong non-linearity of the problem.

Different studies have tackled the Conjugate Heat Transfer (CHT) problem with numerical simulations to handle the heat transfer at the walls. Berger *et. al* [22] performed direct numerical simulations (DNS) of a bluff-body stabilized flame both with fluid only predictions and in a Conjugate Heat Transfer (CHT) context. It turned out that the flame stabilization depended not only on the solid material but also on the initial solution, highlighting that the nonlinear CHT problem can exhibit multiple solutions. The strong effect of heat transfer in bluff-body stabilized flames has also been underlined recently by Fureby [23]. Taking ,gas thermal-radiation and wall Conjugate Heat Transfer into account, LES predictions were in better agreement with experimental data in terms of mean velocity, temperature and CO mass-fraction profiles. The heat loss effects on the stabilization of a lean swirl-stabilized flame close to blow-off conditions was analyzed by Massey *et. al* [24], showing that the lift-off height is influenced by the wall heat transfer modelling. DNS was used to perform a sensitivity analysis of transfer functions of laminar flames [12], proving that the inlet air temperature affects both gas velocity and flame speed whereas the combustor wall-temperature determines the lift-off distance of the flame and controls the FTF delay. The same concept was underlined by Kaess *et. al* [25], who investigated the effect of the thermal wall boundary condition on the FTF of a laminar premixed flame trough LES. Their results showed that the flame anchoring position and the FTF were significantly altered when changing the adiabatic boundary condition to an isothermal boundary condition. In an experimental and numerical work, Chatelier *et. al* [26] showed that one of the main issues that should be taken into account in numerical simulations to capture the thermoacoustic response of a swirled flame is the enthalpy defect impact on the flame structure due to heat losses.

This brief literature review confirms that wall heat transfer effects modify flame stabilization and flame dynamics. Nevertheless, while in experiments this requires a careful attention to the combustor initial conditions to avoid wall-temperature effect and obtain reproducible data, in Computational Fluid Dynamics (CFD) a correct assessment of the wall modelling is required to achieve reliable numerical predictions. If available, measured temperatures can be used as boundary conditions for simulations. However, in most configurations wall-temperature data are difficult to determine and they can change for each operating condition. In many cases, they are just

not available. As a consequence, most CFD simulations either neglect heat-transfer effects, considering the combustor walls as adiabatic (e.g., see Ref [27]) or an arbitrary wall-temperature field is imposed [28–30]. Both approaches still can capture the correct thermoacoustic behaviour as demonstrated in bluff-body stabilized flames [31, 32], lean-premixed swirl flames [27, 30], annular combustion chamber [33] or even rocket combustors [34]. However, these simplistic wall conditions fail when the instability-driving mechanisms are impacted by the unsteady heat-transfer to the walls, and recent studies have underlined how Conjugate Heat Transfer (CHT) can improve the prediction of thermoacustic instabilities. Shahi *et. al* [35] performed numerical simulations of a centerbody stabilized flame both with adiabatic/isothermal boundary wall conditions and with CHT to conclude that the use of the latter led to significant accuracy improvements in the prediction of the characteristics of the combustion instability. For a swirled-flame combustor, Kraus *et. al* [7] discussed the potential of CHT simulations to improve LES accuracy for the prediction of combustion instabilities in terms of frequency and amplitude of the oscillations due to the strong preheating of the gases in the combustor plenum.

In general, it is possible to classify the approach toward heat-transfer in four categories of increasing complexity, based on the thermal boundary conditions imposed at the walls [7]:

1. Adiabatic walls: in most recent LES the walls are considered as adiabatic and heat transfer is neglected [27, 31–33].
2. Imposed wall-temperature: when experimental data includes wall temperatures, it is possible to fix the temperature directly through Dirichlet boundary conditions [36, 37].
3. Imposed local thermal resistance: the local heat flux Φ_q can be computed from a reference temperature T_{ref}, the temperature of the fluid at the wall T_f provided by the simulation and a suitable thermal resistance R which takes into account the conduction through the solid [6, 38] and the external convection and radiation [4]: $\Phi_q = (T_f - T_{ref})/R$.
4. Conjugate Heat Transfer (CHT): the LES solver can be coupled with a code that solves for heat conduction in the solid parts of the combustor: the wall heat conduction and the unsteady flow solvers run in parallel and exchange values of wall-temperatures and heat flux at the boundaries [23, 35, 39].

Among the different gas turbine model combustors, the PRECCINSTA test bench is one of the most well-known in the combustion community: this test rig, derived from an industrial design by Safran Helicopter Engines and operated by DLR [40], has been widely investigated both trough experiments [40–43] and numerical simulations [1, 2, 28, 44–52]. Most studies refer to the stable flame case (equivalence ratio of $\phi = 0.83$ and thermal power of $P_{th} = 30$kW) and the unstable flame case with a thermoacoustic limit cycle at 290 Hz ($\phi = 0.7$ and $P_{th} = 25$ kW) observed by Meier *et al.* [40]. To the author's knowledge an analysis of the heat transfer impact on the thermoacoustic behavior of this test rig has never been performed. The analysis of the thermoacoustic oscillation performed via compressible LES by Roux *et al.* [1] and Franzelli *et al.* [44] were conducted for adiabatic walls, achieving good prediction of the oscillation mode but marginal agreement for the frequency of oscillation. More studies have focused on the impact of detailed chemistry [45], sub-grid scale closure for premixed turbulent combustion [2] and combustion TFLES model with a dynamic wrinkling formulation [51]. The first study that introduced heat losses at the walls in the PRECCINSTA test rig was conducted by Bénard *et al.* [28] in the context of a mesh sensitivity analysis in the stable flame regime. To do so the authors imposed a numerically-tuned temperature profile at the combustor walls and backplane to match the experimental fluid temperature profiles [40], but the centerbody on which the flame stabilizes was kept adiabatic. A similar approach has been recently used also by Fredrich *et al.* [46, 52], who proposed to detect the thermoacoustic instability with a fully-compressible LES-pdf approach. To take into account the heat losses, they fixed the chamber walls at a guessed temperature of 1400 K and the backplane at 700K, following the experimental data of Yin *et al.* [43]. However, using the same experimental data for the centerbody, they claimed that prescribing a wall-temperature of 700 K caused the flame to consistently lift off and fully detach from the nozzle and therefore assumed an adiabatic condition. It is important to note that the experiments conducted by Yin *et al.* [43] refer to different operating conditions with respect to the one simulated by Fredrich *et al.* [46, 52], potentially explaining the lift-off of the flame. In all these studies, since a pre-heating of the gases before entering the combustion chamber was experimentally observed to reach values between 320 K and 380 K, although not precisely measured [40], the temperature of the fresh gases has been set to 320 K instead of the ambient temperature. To conclude, the lack of a clear and systematic analysis of the heat losses in this test rig can be due to two main factors: (a) the lack of experimental data of wall-temperatures (some measurements at the backplane and centerbody tip have been recently performed by Yin *et al.* [43] but in operating conditions different from the ones of Meier *et al.* [40]) and (b) the satisfactory agreement of LES predictions with adiabatic boundary conditions. This work addresses this issue by performing a systematic study of the impact of heat transfer in the PRECCINSTA test bench. Note that a new test campaign was conducted at DLR where the test rig was operated in different operating conditions with respect to the data available in the literature [40, 43].

In the following, the experimental setup, the observed flame shape and thermoacoustic behavior are first presented together with the numerical setup and the AVBP LES solver, section 2. Results are discussed in section 3. First, the Heat Resistance Tuning (HRT) approach for the thermal boundary condition determination using experimental measurements is presented in section 3.1. Second, since with the HRT approach the predicted flame becomes unstable and responds to a thermoacoustic oscillation that is not observed experimentally, a Conjugate Heat Transfer (CHT) simulation is discussed in section 3.2 after having presented the heat conduction AVTP solver. Finally, the instability-driving mechanism is physically investigated to

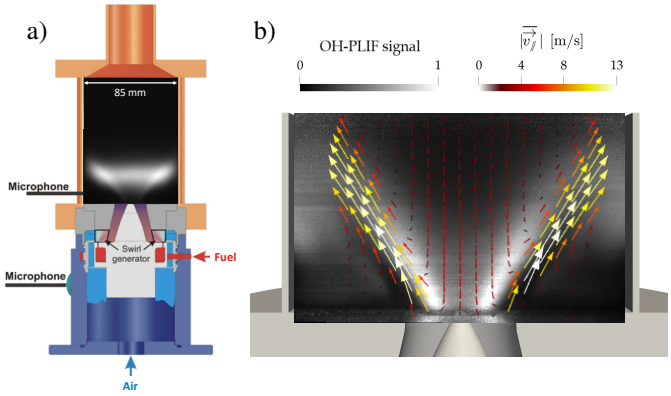

Figure 1: (a) Schematic of the experimental test bench: injector with combustion chamber and normalized time-averaged Line-Of-Sight (LOS) OH* chemiluminescence indicating the flame; (b) Experimental normalized time-averaged OH-PLIF image. The arrows are tangential to the experimental time-averaged velocity field in the plane $\overrightarrow{v_{//}}$, their length and color indicating the velocity magnitude.

understand the differences between the HRT approach and the CHT predictions in section 3.3.

2. Experimental and numerical setup

A schematic of the PRECCINSTA experimental test bench [40] is presented in Fig. 1(a) showing the injector and the combustion chamber, together with the experimental normalized time-averaged Line-of-sight (LOS) OH* chemiluminescence image. Dry air is fed at ambient temperature through the plenum and a swirl motion is imposed thanks to 12 radial swirler vanes before entering the combustion chamber. Methane is injected into the air stream through small holes within the radial swirler in a partially premixed mode. The high momentum ensures good mixing before entering the combustion chamber even if local equivalence ratio variations have been reported in the literature [40]. The combustion chamber has a square section of 85 x 85 mm^2 and quartz windows (thickness 1.7 mm) to allow for optical access for diagnostics. At the end of the combustion chamber, the hot gases exit through a cone-shaped exhaust pipe.

The test rig has been recently been operated at different operating conditions to analyze the effects on flame dynamics. In this work, an experimentally stable condition is computed for a global equivalence ratio of $\phi = 0.8$ ($\dot{m}_{air} = 4.29$ g/s and $\dot{m}_{CH_4} = 0.2$ g/s) and a thermal power of $P_{th} = 10$ kW. Measurements of the three velocity components were performed in one vertical plane along the radial direction using Stereoscopic Particle Image Velocimetry (sPIV). Planar Laser-Induced Fluorescence (PLIF) measurements of OH radicals are used to visualize the flame structures together with line-of-sight integration of OH* chemiluminescence, which represents a qualitative indicator for the heat release rate for lean premixed flames [53].

The experimental normalized time-averaged OH-PLIF image on a vertical plane is presented in Fig. 1(b) together with the

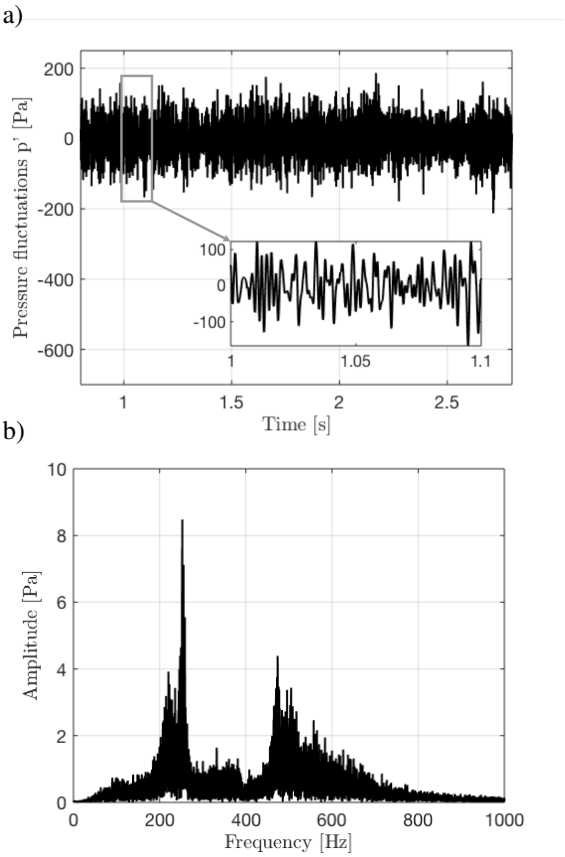

Figure 2: (a) Experimental pressure recorded at the combustion chamber backplane with a zoom on a part of the signal and (b) the signal spectrum obtained via Fast Fourier Transform (FFT).

experimental time-averaged velocity field in the plane, $\overrightarrow{v_{//}}$, indicated by the arrows which are tangential to the velocity vector and colored by its magnitude. A classical swirled flow structure of the velocity field can be observed. A strong Central Recirculation Zone (CRZ) downstream of the centerbody helps the flame stabilization by bringing back the hot burnt gases toward the flame root and weaker Outer Recirculation Zones (ORZs) are also present. Starting from the injector exit, the intense jet flow exiting from the swirler prevents flame anchoring: the flame is stabilized in the low-velocity region near the end of the CRZ close to the centerbody (note the metallic tip visible in the image) and it develops further downstream in a V-shape reaching the chamber walls at around 50 mm from the backplane where it quenches due to wall heat losses. A weaker signal is observed in the ORZs with respect to the primary zone close to the centerbody, indicating that the flame is not always present in these regions (as expected in a V-shape flame).

Figure 2 reports (a) the pressure recorded experimentally at the combustion chamber backplane and (b) its spectrum computed using a Fast Fourier Transform (FFT) algorithm. Two weak modes appear at 260 Hz and 480 Hz: these frequencies match the first two acoustic modes of the system (see section. 3.3). The weak amplitude of the two pressure peaks (smaller than 10 Pa) indicates that no thermoacoustic activity takes place for these operating conditions.

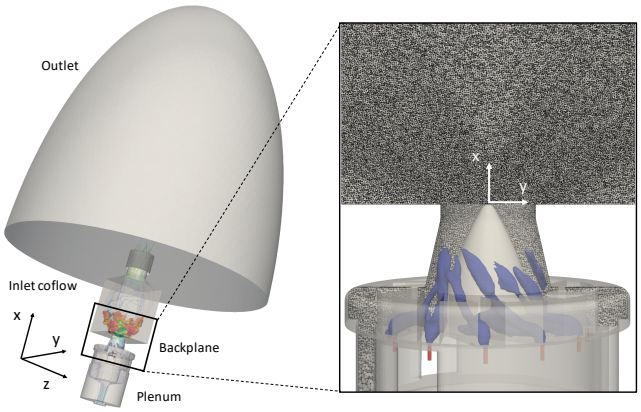

Figure 3: Computational domain used in LES with an overview of the mesh and the used coordinate system. Note that in LES the atmosphere is taken into account and the inlet fuel geometry is simplified to the 12 small tubes (colored in red) without the fuel plenum. The instantaneous isocontour of CH_4 (colored in blue) helps visualize the technical fuel injection in the swirled flow.

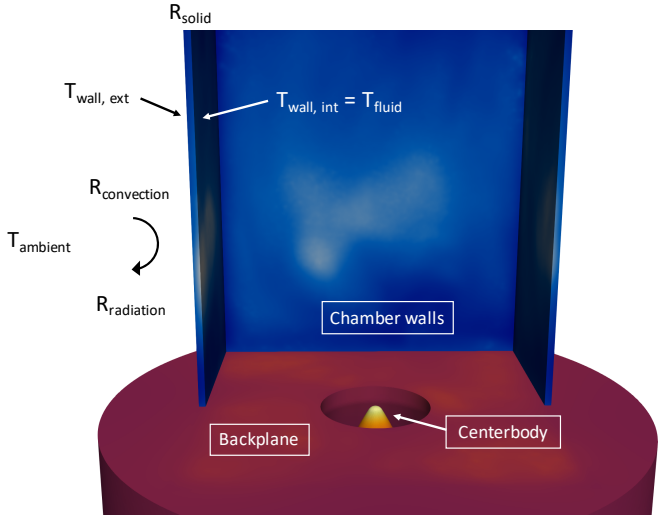

Figure 4: Schematic showing the different heat losses mechanisms at the combustor chamber walls and respective thermal resistances.

The LES domain is shown in Fig. 3 with an overview of the unstructured grid: the outside atmosphere is taken into account to have the right impedance at the outlet of the combustion chamber and the inlet fuel geometry is simplified into 12 small tubes (colored in red) without the fuel plenum. In Fig. 3, an instantaneous isocontour of CH_4 is colored in blue to help visualize the technical fuel injection in the swirled flow. LES are performed using the AVBP code (www.cerfacs.fr/avbp7x/index.php) solving the compressible Navier-Stokes multi-species equations. The SIGMA turbulent closure is used for the sub-grid stresses [54] and the TTGC scheme (third order in time and space) is used for the discretization of the convective terms [55]. Inlet and outlet boundary conditions are treated with the Navier-Stokes Characteristic Boundary Conditions (NSCBC) formalism [56] with a relaxation factor of $K_{air} = 50\ s^{-1}$ and $K_{fuel} = 5 \times 10^5\ s^{-1}$ imposed on the air and fuel inlets, respectively. All walls are treated as no-slip. Two of the four treatments listed in the introduction are compared. At first, a simplified HRT approach is proposed (see section 3.1). Results will be compared with predictions from a more reliable, but also more computationally demanding, fully coupled Conjugate Heat Transfer case (see section 3.2). Both cases are performed using the same computational grid of 20.3M tetrahedral elements which was optimized applying static mesh refinement criteria [57]. The final grid uses a mesh size in the flame zone just downstream of the centerbody of $\Delta_x = 300\mu m$, assuring an almost unity y^+ value at the centerbody tip and $y^+ \sim 3$ at the chamber and backplane walls, hence allowing the use of a wall resolved LES approach. A proper mesh resolution at the walls is of fundamental importance to correctly estimate the thermal fluid boundary layer and hence the convective heat transfer at the walls. The dynamic formulation of the thickening flame model (DTFLES) [58] is used to resolve the flame. The model is coupled to the Charlette efficiency function [59] used with the standard coefficient $\beta_{Ch} = 0.5$ to retrieve flame-turbulence interaction. CH_4-Air chemistry is described through an Analytically Reduced Chemistry (ARC) mechanism consisting of 20 transported species, 166 reactions, and 9 quasi-steady state species, derived from the detailed GRI-Mech 3.0 scheme [60] and already validated for the PRECCINSTA flame [57]. More details about this scheme are provided in the supplementary materials of Ref. [38]. The thermal radiation from the hot gases is taken into account by the LES solver with the Optically Thin Assumption (OTA) [61] for the most radiating species CH_4, CO, CO_2, and H_2O: gases are supposed to be optically thin and reabsorption is neglected while the Planck mean-absorption coefficients are provided for each species as polynomial functions of temperature [62].

3. Results and discussion

LES results obtained with the HRT (section 3.1) and CHT approaches (section 3.2) are first compared, illustrating the impact of the wall boundary conditions for the current configuration. Then, the instability-driving mechanisms are investigated to understand the differences between the two approaches (section 3.3).

3.1. Heat Resistance Tuning (HRT) approach

The first approach consists of imposing a heat flux (Φ_q) at each point of the wall. The wall heat flux Φ_q is defined as $\Phi_q = (T_f - T_{ref})/R$ where T_{ref} is a reference temperature (usually the air temperature in the room or the external wall-temperature), T_f is the temperature of the fluid at the wall and R is a thermal resistance. While it is generally easy to set the reference temperature T_{ref}, defining a correct value for the resistance R is not straightforward and depends on the heat transfer at the combustion walls.

If the experimental temperature on the external side of the chamber walls ($T_{wall,ext}$) is available (see Fig. 4) and, therefore, chosen as T_{ref} in the calculation of Φ_q, the thermal resistance

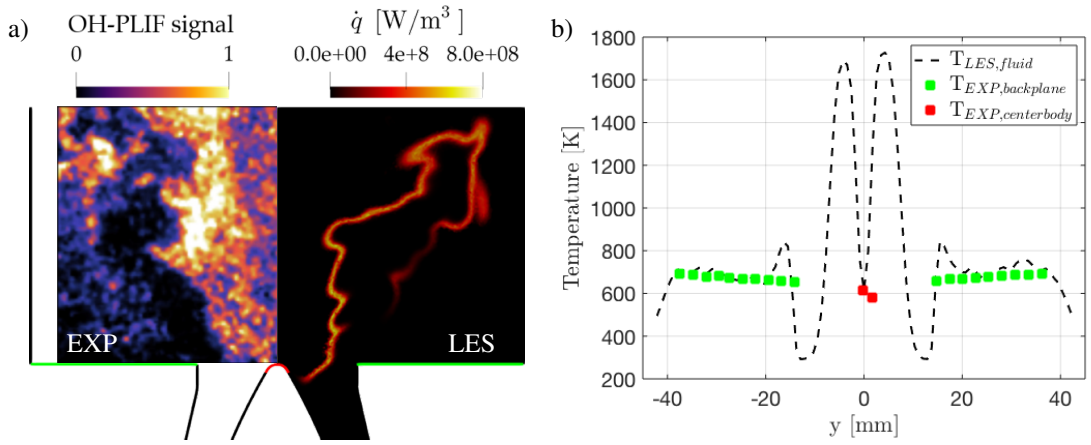

Figure 5: (a) Comparison of experimental instantaneous normalized OH-PLIF signal and instantaneous predicted heat release rate $\dot{q}$. Green and red lines indicate experimental data location at the backplane and centerbody tip respectively. (b) Comparison of experimental and LES profiles of mean temperature at the combustion chamber backplane and centerbody tip after tuning of the heat resistances. Condition $P20_{CB}$: P_{th} = 20KW and ϕ = 0.7 [43].

Case	P_{th}	ϕ	Exp. data	Ref.
$P20_{CB}$	20KW	0.7	$T_{backplane}$, $T_{centerbody}$	Yin *et al.* [43]
$P30_W$	30KW	0.83	T_f	Meier *et al.* [40]
$P10$	10kW	0.8	-	Present study

Table 1: Summary of the operating conditions considered in the HRT approach.

is fixed by the solid R_{cond} which takes into account heat conduction inside the chamber walls [6, 38]. In general, however, experimental data of wall-temperatures is not available (or incomplete). In these cases, a possible solution is to consider the ambient temperature as reference T_{ref} but doing so an additional thermal resistance should be added to R_{cond} to take into account the external heat losses due to natural (or forced) convection (R_{conv}). Expressions of this resistance can be found in the literature as correlations of the Nusselt number based on geometrical dimensions, Prandtl and Rayleigh (Reynolds) number for natural (forced) convection [63, 64].[1] can be considered to act in parallel to the convection. Similarly to an electric circuit, an equivalent resistance can be defined as $R_{eq} = R_{cond} + \frac{1}{1/R_{conv} + 1/R_{rad}}$. See Appendix A for a more detailed discussion.

In PRECCINSTA, experimental temperatures were measured by Yin *et al.* [43], who provided the surface temperature of the backplane and the centerbody tip for an operating condition with a thermal power P_{th} = 20KW and an equivalence ratio ϕ = 0.7 (in the following referred to as case $P20_{CB}$ where the subscripts stands for *centerbody*) which is different from the operating condition selected for the current study (in the following referred to as case $P10$). The other temperature measurements available refer to flow temperature profiles measured by Meier *et al.* [40] for operating conditions with a thermal power P_{th} = 30KW and equivalence ratio ϕ = 0.83 (in the following referred to as case $P30_W$ where the subscripts stands for *walls*). The operating conditions and experimental data available are summarized in Table 1.

Even if this was done in previous publications, due to the thermal power differences, none of these measurements can be directly used for T_{ref} in the present study since wall surface temperatures cannot be considered independent of the global thermal load. On the contrary, thermal resistances are an intrinsic property of the system (determined by the rig geometry, wall material properties and, if present, cooling systems) and, as a first approximation, can be assumed not to change significantly while changing operating conditions[2]. The fact that measurements of wall-temperature at few regimes can be used to determine local wall heat resistances, valid for all regimes, is the basis of the Heat Resistance Tuning (HRT) approach used here: case $P20_{CB}$ is simulated first and the thermal resistances of the backplane and centerbody are tuned to match the surface temperature measurements. The same exercise is then reproposed for case $P30_W$ retrieving the optimized resistance for the chamber walls. Before the iterative tuning procedure, the initial guess of the thermal resistances has been set for each surface as an equivalent resistance R_{eq} computed following the depicted methodology and making use of standard correlations. More information can be found in Appendix A. In both simulations, other walls are assumed to be adiabatic since no relevant heat transfer is expected. Note that to take into account the experimentally observed pre-heating of the flow in the plenum, the inlet temperature of the flow (and hence also T_{ref}) is imposed to 320K as proposed by Franzelli *et al.* [44].

The outcome of the HRT procedure for case $P20_{CB}$ is presented in Fig. 5. For this particular condition, the flame experimentally showed intermittent transitions between V- and M-shapes with an effect on the surface temperature of the backplane and centerbody. In our case, LES predicts a V-shape, as seen in Fig. 5(a) which compares the experimental instantaneous normalized OH-PLIF signal with the instantaneous pre-

[1] In the same manner, a thermal resistance that accounts for radiation R_{rad}

[2] Of course thermal resistances are also dependent on the surface temperature since the latter affects the solid thermal conductivity, the radiation and the convection but these effects can be assumed to be negligible as a first approximation for small variations of surface temperature.

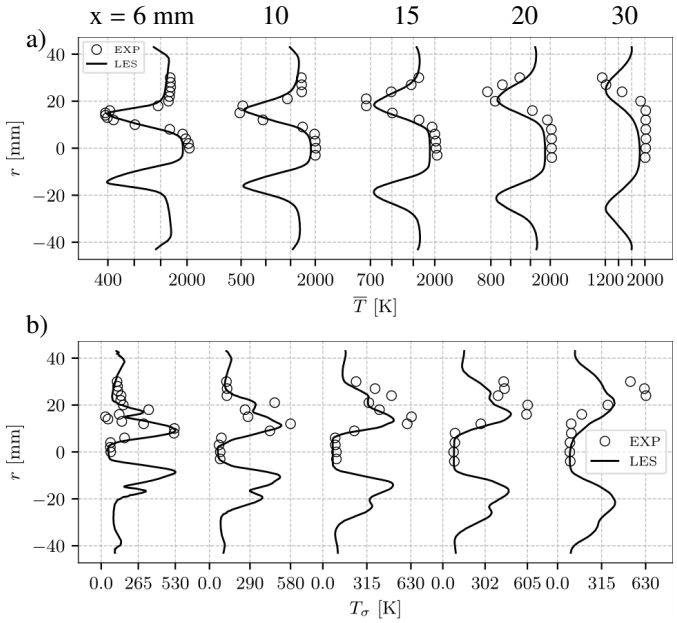

Figure 6: Comparison of experimental and predicted profiles of (a) mean and (b) RMS temperature at measurement planes at x = 6, 10, 15, 20 and 30 mm downstream of the combustion chamber backplane for tuning the thermal boundary conditions at the chamber walls. Condition $P30_W$: P_{th} = 30KW and ϕ = 0.83. [40]

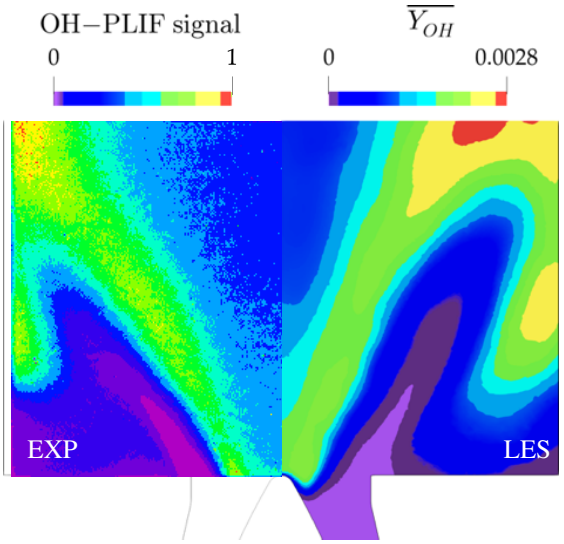

Figure 7: Comparison of experimental time-averaged normalized OH-PLIF signal and time and angle-averaged predicted OH mass fraction $\overline{Y_{OH}}$. Case $P30_W$: P_{th} = 30KW and ϕ = 0.83 [40].

dicted heat release rate $\dot{q}$. The LES flame is attached to the centerbody and detached from the backplane, with a weaker heat release rate in the ORZ, as in the experiments. The HRT procedure is performed using the measured surface temperature for the V-shape flame. The outcome of HRT is presented in Fig. 5(b) showing the comparison of experimental and predicted profiles of mean temperature at the backplane and at the centerbody tip. The final values of the thermal resistances $R_{backplane} = 4.3 \times 10^{-3}$ m^{2}K/W and $R_{centerbody} = 7.5 \times 10^{-3}$ m^{2}K/W allow LES to reproduce the measured thermal state at the walls. The temperature of the centerbody tip reaches 600 K and the backplane wall 650 K in LES while experimental measurements are 580 to 610 K and 630 to 670 K for the centerbody tip and chamber backplane, respectively. The simulation (Fig. 5(b)) predicts a locally higher temperature at ± 17 mm with respect to the experiments. This difference highlights a limitation of the HRT approach: in reality the solid conductivity (which is notably higher with respect to the fluid one) transfers more efficiently the heat from the hot spots to the colder regions thanks to transversal diffusion resulting in a more uniform temperature in the solid (i.e. typically the Biot number[3] is much lower than unity [7, 65]). However, this feature cannot be correctly reproduced by the HRT approach which assigns a single thermal resistance value for the whole surface[4].

Once thermal resistances for backplane and centerbody have been fixed, case $P30_W$ is simulated to tune the thermal resistance at the combustion chamber walls. Bénard *et al.* [28] conducted a similar tuning on the same case to find the temperature profile to be imposed at walls with a Dirichlet boundary condition. However, it is worth re-affirming that imposing a fixed temperature field is not appropriate in reactive LES for two reasons and that HRT is more powerful. First, temperature is an output of the simulation and its profile on the wall should depend on the evolution of the flow field and flame shape during the simulations. If a fixed temperature profile is rigidly imposed, the model will not be able to correctly capture temperature wall variations due to eventual interactions of the flame with the wall. Furthermore, since the wall surface temperature is case dependent, the procedure proposed by Bénard *et al.* [28] cannot be used for other operating conditions. The HRT strategy, relying on thermal resistances, is more general.

Results are presented in Fig. 6, which shows experimental and predicted profiles of (a) mean and (b) RMS temperature at different measurement planes downstream of the chamber backplane with the resulting value of $R_{walls} = 7 \times 10^{-2}$ m^{2}K/W. The LES temperature field is in good agreement with the experimental one. A small difference between LES and experiments is visible at the last profile (h = 30 mm) downstream of the backplane: the mean temperature field shows that the flame angle is slightly underestimated in this case and a lower temperature RMS peak is predicted. These differences can be explained by experimental uncertainties and by the fact that the tuning procedure does not rely in this case on a measured surface temperature (as in case $P20_{CB}$) but on the flow temperature, which adds further uncertainties.

The comparison between experimental time-averaged normalized OH-PLIF signal and time as well as angle-averaged

[3] $Bi = hL/\lambda$ where h is the convective heat transfer coefficient, L the characteristic length and λ the thermal wall conductivity. In the current operating conditions, the convective heat transfer at the backplane is low due to low velocity (~ 2 m/s) in the ORZ, making the conduction heat transfer more efficient.

[4] Although imposing a spatial distribution of thermal resistances for each surface is possible, it is in practice difficult to validate due to the marginal amount of experimental data available and it is therefore out of the scope of the present work.

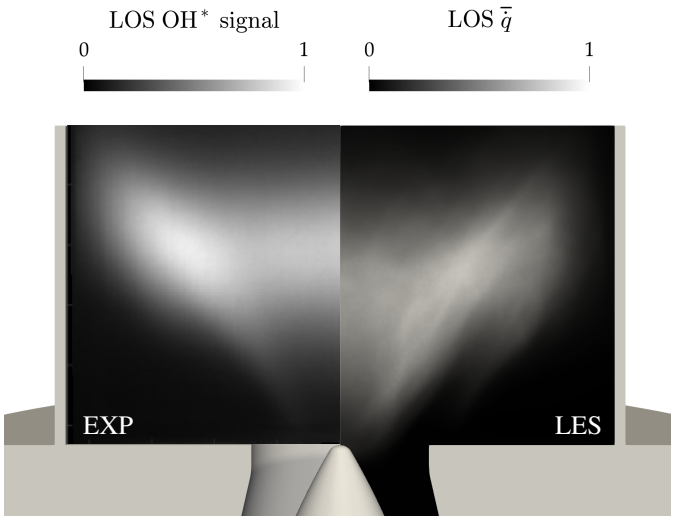

Figure 8: Validation of the LES simulations with HRT approach for case $P10$. Comparison of experimental normalized time-averaged LOS OH* chemiluminescence image with LOS of predicted heat release rate $\overline{\dot{q}}$.

LES predicted OH mass fraction $\overline{Y_{OH}}$ in case $P30_W$ is presented in Fig. 7. A correct V-shape flame is predicted by LES and global good agreement is achieved in terms of flame length and angle. The ORZs present weaker OH signal and the flame lift-off from chamber backplane is captured. The HRT also predicts a well-attached flame at the centerbody thanks to the correct heat resistance used for the centerbody walls (also tuned from case $P20_{CB}$). Generally speaking, this result confirms the relevance of the HRT approach for variable operating conditions: predicted wall-temperatures vary as the regime changes. The centerbody tip temperature reaches a value of around 900 K for case $P30_W$, notably higher than the one measured in condition $P20_{CB}$ of 600 K (which has a lower equivalence ratio $\phi = 0.7$ and a lower thermal power compared to case $P30_W$). This may explain why Fredrich *et al.* [46, 52] did not observe an attached flame at the centerbody by prescribing the same wall-temperature as in case $P20_{CB}$ of Yin *et al.* [43].

The HRT approach is then applied to case $P10$, which is the final objective of the present study. The mean LOS predicted heat release rate $\overline{\dot{q}}$ is compared with the experimental normalized time-averaged LOS OH* chemiluminescence in Fig. 8. LES captures the mean flame angle while the flame length is slightly underestimated. A global satisfactory agreement is achieved in terms of flame shape with the HRT approach, the only main difference being the region of heat release rate in the CRZ which is not observed in experiments.

Even though the mean flame is reasonably captured using the HRT method, the limits of this approach become visible when the flame dynamics are considered. Indeed, differences with the experiment can be noticed for heat release rate fluctuations and pressure oscillations predicted at the combustion chamber backplane shown in Fig. 9(a): unlike experimental recordings of Fig. 2, high amplitude pressure oscillations of $p'_{num} \simeq 800$ Pa (to be compared with experimental ones of $p'_{exp} \simeq 200$ Pa) are predicted by LES. Furthermore, the phase difference between

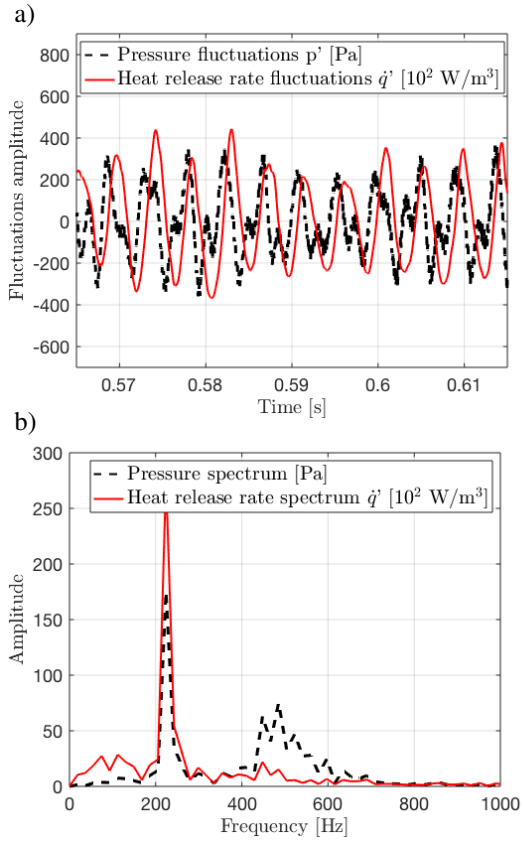

Figure 9: (a) Pressure and heat release rate fluctuations predicted at the combustion chamber backplane using the HRT approach. The phase difference between the unsteady pressure and heat release rate oscillations is less than $\pi/2$, satisfying the Rayleigh criterion. (b) Signals spectra via FFT, showing that heat release rate fluctuations correspond to a peak at 224 Hz, while pressure spectrum shows also a second peak at 480 Hz.

the unsteady pressure (black line) and heat release rate (red line) oscillations is within the $\pi/2$ limit, satisfying the well-known Rayleigh criterion [66]. This hypothesis is further confirmed by the spectrum of the two signals shown in Fig. 9(b): differently from the experimental observations (Fig. 2(b)), a strong peak almost one order of magnitude higher than in the experiments is observed in both heat release rate (red line) and pressure (black line) spectra at 224 Hz, indicating that the instability is fed by a flame/acoustics coupling. A second peak is also present in the pressure spectrum at 480 Hz.

To understand the dynamics of this numerically-predicted thermoacoustic oscillation, Fig. 10 shows the phase-locked instantaneous fields of axial velocity (left) and CH4 mass fraction (right) with the heat release rate fields $\dot{q}$ for four different phases of the heat release rate oscillating cycle at 224 Hz. Figures 10(a-c) correspond to the minimum ($\varphi = 0$) and maximum ($\varphi = \pi$) of the heat release rate in the cycle, respectively. The other two phases shown in Figs. 10(b-d) refer to instants at $\varphi = \pm\pi/2$ respectively. In all images, the black isocontours refer to temperature levels of 750 and 1500 K whereas the white isocontour refers to the CH_4 global mass fraction level corresponding to $\phi = 0.8$. When the heat release rate is minimum in Fig. 10(a) (that corresponds to a minimum in the plenum pres-

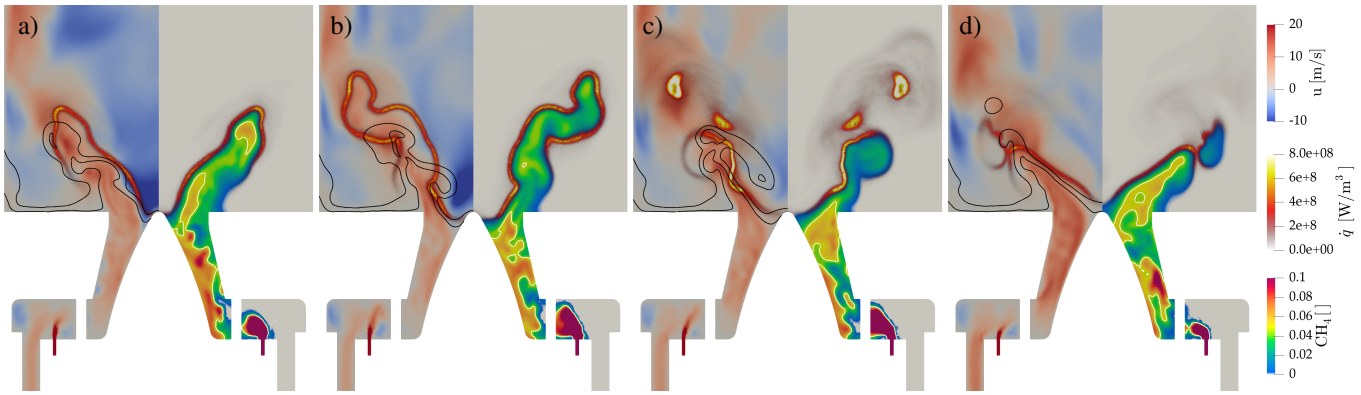

Figure 10: Phase-locked instantaneous fields of axial velocity (left) and CH_4 mass fraction (right) with superimposed the heat release rate field $\dot{q}$ for four different phases of the oscillating cycle. (a) and (c) correspond to the minimum and the maximum of heat release rate in the cycle, respectively. Black isocontour refer to temperature levels of 750 and 1500 K while white isocontour refer to the CH_4 global mass fraction level.

sure), the axial velocity in the swirler is low, with a strong CRZ downstream of the centerbody. The CH_4 jets are injected in a low velocity air stream and are not significantly forced toward the centerbody walls. After $\varphi = \pi/2$ (Fig. 10(b)), the CRZ is still present in the chamber and the velocity in the swirler is still low: CH_4 accumulates in the swirler and pockets of higher ϕ are visible close to the centerbody. At the same time the flame gets longer because the equivalence ratio ϕ before the flame is now lower than the global value (i.e. the white isocontours are far from the flame front). At $\varphi = \pi$ (Fig. 10(c)), when heat release rate and plenum pressure are maximum, the velocity in the swirler is high and starts to push the CH_4 jet downstream. At the same time the previous injected fuel-rich pocket has reached the flame front, which gets shorter and burns at the maximum of the heat release rate. Finally, at $\varphi = -\pi/2$ (Fig. 10(d)), the velocity in the swirler is at its maximum, causing the fuel jet to be strongly pushed toward the centerbody.

This thermoacoustic feedback loop resembles the one effectively present in the experiments conducted by Meier *et al.* [40] for $\phi = 0.7$ and $P_{th} = 25$ kW and is explained by the mechanism described by Franzelli *et al.* [44] using LES: the velocity field in the swirler follows the plenum pressure and oscillates, causing rich gas pockets to be periodically pushed into the chamber and producing fluctuations of the heat release rate. The fuel enters the swirl channel as a jet-in-crossflow and, depending on the momentum flux ratio, may impinge on the walls. This flapping of the fuel jet is less evident if compared to their LES but still noticeable. However, differently from the experiments of Meier *et al.* [40], this mechanism is not triggered experimentally for the studied case $P10$ and possible causes for its appearance are investigated hereafter.

One possible reason explaining why LES seems unstable is acoustic damping [67]. In the absence of additional passive damping such as Helmholtz resonators, the main contributor to damping is the losses of acoustic energy at the boundaries of the system [50, 68]. In LES, inlet and outlet boundary conditions are treated with the classical Navier-Stokes Characteristic Boundary Conditions (NSCBC) formalism [56]. According to the NSCBC theory [56, 69], the inlet and outlet reflection coefficients $\mathcal{R}$ are functions of the frequency and of the relaxation coefficient K used [70] to avoid that mean values drift away from their target values. At the outlet, including the atmosphere in the computational domain assures the correct representation of the acoustic impedance at the exit of the combustion chamber. A systematic analysis of the effect on the thermoacoustic oscillation amplitude of only the relaxation coefficients imposed at the air and fuel inlet lines was conducted. These K coefficients control the "stiffness" of the air and fuel lines which are unknown and may explain LES/EXP discrepancies. Figure 11 shows the fluctuations of (a) heat release rate, (b) pressure signal at the chamber backplane, (c) air mass flow rate and (d) fuel mass flow rate for different values of K. For a given value of $K_{air} = 50$ s^{-1} (soft air line), two different $K_{fuel} = 5 \times 10^3$ s^{-1} (soft fuel line) and $K_{fuel} = 5 \times 10^5$ s^{-1} (stiffer fuel line) are tested (continuous and dashed lines in Fig. 11). No difference can be detected between these two cases for heat release rate, pressure or air mass flow rate. On the contrary, a higher impact can be observed when K_{air} is increased to 5×10^3 s^{-1} making the air line stiffer keeping $K_{fuel} = 5 \times 10^3$ s^{-1} constant (continuous line with rectangular marks in Fig. 11). The amplitude of (a) heat release rate and (b) pressure oscillations increase while the frequency slightly increases to 244 Hz. The oscillation of the air mass flow rate (c) is instead lower if compared to the cases at $K_{air} = 50$ s^{-1} since with a higher relaxation coefficient the boundary tends more rapidly to the mean target value ($u \rightarrow \bar{u}$) with an acoustic behaviour closer to a velocity node ($u' = 0$). In this configuration, fuel mass flow rate oscillations (Fig. 11(d)) slightly increase (0.01 g/s, i.e., 5% of the mean value) with a negligible impact on the instability amplitude. With a further reduction of K_{fuel} no significant change has been observed while a mean value drift occurred (not shown). As a final test, an almost anechoic condition is imposed at the inlet further reducing K_{air} to 5 s^{-1}: in this case, the amplitude and the frequency of oscillations for both heat release rate and pressure are unaffected by changes of K (dashed line with circular marks in Fig. 11).

These observations show that for case $P10$, the impedance of the fuel line (controlled by K_{fuel}) has no relevant impact on

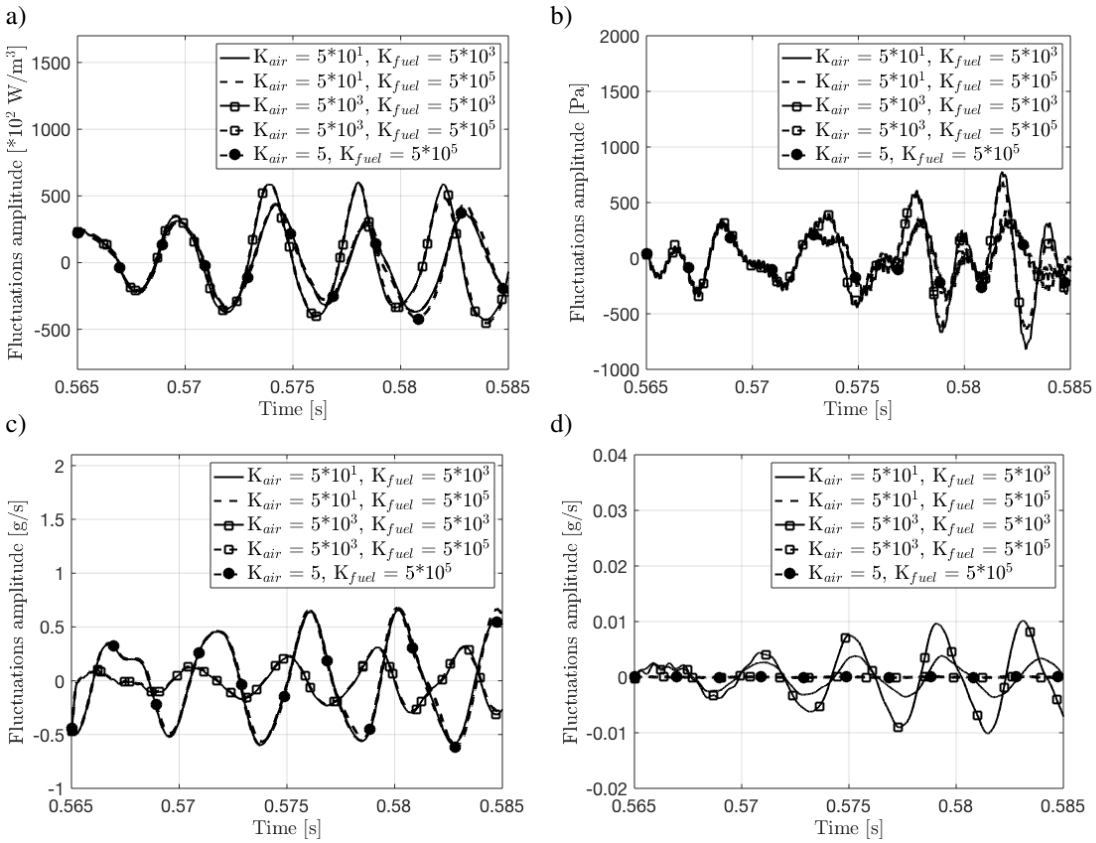

Figure 11: Effect of the acoustic impedance of the air and fuel lines. Predicted fluctuations of (a) heat release rate, (b) pressure signal at the combustion chamber backplane, (c) air mass flow rate and (d) fuel mass flow rate.

the predicted thermoacoustic oscillations[5]. This could be explained by the small fuel tube sections compared to the swirler dimensions that create acoustic reflections due to the cross section change [71]. A higher impact is observed when changing the air inlet line impedance (controlled by K_{air}). Nevertheless a stabilization of the observed thermoacoustic mode was never reached even when an almost anechoic boundary is imposed. An underestimation of the acoustic damping is therefore not responsible for the thermoacoustic oscillations observed in the simulations with the HRT approach. Even if HRT reproduces the mean flame shape reasonably, it fails to characterize its unsteady dynamics.

3.2. Conjugate heat transfer (CHT) approach

To remove uncertainties on the heat transfer between the fluid and the solid, CHT simulations are performed by coupling the LES solver with the AVTP code [72, 73] which solves for heat conduction in the walls of the chamber using the energy conservation equation,

$$\rho_s C_s \frac{\partial T(x_i,t)}{\partial t} = -\frac{\partial \Phi_{q,i}}{\partial x_i}, \tag{1}$$

where ρ_s and C_s are the solid density and heat capacity respectively, T is the solid temperature and $\Phi_{q,i}$ is the conduction heat flux described by Fourier's law,

$$\Phi_{q,i} = -\lambda_s \frac{\partial T}{\partial x_i}, \tag{2}$$

and is controlled by the heat conductivity of the solid λ_s. AVTP takes into account local changes of λ_s and C_s due to the different materials of the rig (e.g. inconel, quartz, etc) and to the local temperature.

AVTP is coupled with the LES solver AVBP through a Parallel Coupling Strategy (PCS) in which both solvers run together and exchange information at each coupling iteration by using the CWIPI library [74]. In the AVBP/AVTP case, the LES solver uses the solid surface temperature T_s as boundary conditions at the walls computed by AVTP while the latter uses the heat flux Φ_q computed by AVBP. The time step at which the two codes advance are different: in AVBP, the time step δt is limited by the Courant-Friedrichs-Lewy (CFL) condition, which for a typical resolution of the fluid mesh brings to a time step δt_f of the order of 10^{-8} s. In AVTP, the time step is controlled by

[5] Franzelli *et al.* [44] predicted in the pulsating flame of Meier *et al.* [40] an oscillating frequency of 390 Hz which was higher than the experimental value of 290 Hz. This discrepancy was attributed to the acoustic impedance of the fuel line which was arbitrarily imposed in LES. The present analysis would suggest instead (for different operating conditions and hence pressure oscillations levels) that the impedance of the fuel line has no impact on the thermoacoustic instability and that the higher predicted frequency of oscillation was due to the adiabatic walls (i.e. higher sound speed) and to the K_{air} coefficient which has an impact on the frequency.

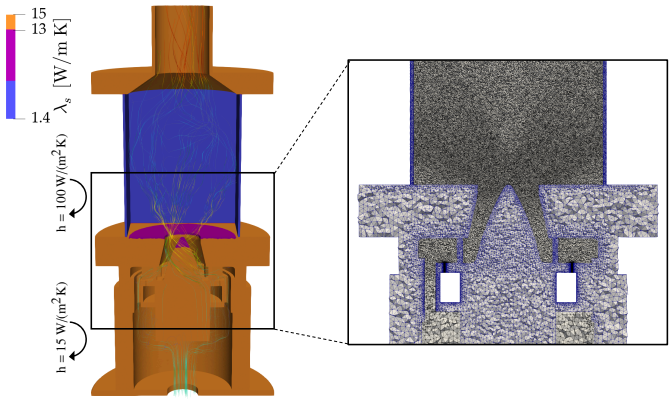

Figure 12: Computational domain used in CHT simulations with overview of the solid (blue) and fluid (black) meshes with thermal boundary conditions for the AVTP code. Assumed thermal conductivity λ_s for quartz (blue), inconel (purple) and stainless steel (orange) is also indicated.

the Fourier number and leads to a time step δt_s of the order of 10^{-5} s. It is possible to synchronize the two solvers by changing the number of iterations that each of them performs in between two consecutive coupling iterations (i.e. at the information exchange time). Note also that the characteristic time of the flow τ_f (i.e. the flow-through time) is typically much smaller than the characteristic time of the heat transfer in the solid τ_s. The first can be computed as $\tau_f = \rho V/\dot{m}$ where ρ is the mean flow density, V is the volume of the combustion chamber and $\dot{m}$ is the mass flow rate and τ_f is typically of the order of milliseconds. The characteristic time of the heat transfer in the solid τ_s [65] can be computed as $\tau_s = V_s\rho_s C_s/hS$ where S is the surface area, V_s and ρ_s are the volume and the density of the solid and h is the heat transfer coefficient: hence τ_s is of the order of 1 - 10 s. The difference between τ_s and τ_f would lead to very long CPU time for the flow solver if the two solvers are synchronized in time. To speed up the convergence toward a solid steady state temperature, the two solvers can be de-syncronized in time by increasing the number of iterations performed by AVTP with respect to AVBP between two consecutive coupling iterations. This methodology is equivalent to decreasing the heat capacity of the solid and, hence, the characteristic time of the heat transfer in the solid τ_s. Once a steady state is reached (i.e. statistical convergence), the two solvers can be re-synchronized in time.

The computational domain used in CHT AVBP-AVTP simulations is presented in Fig. 12 where the solid mesh is blue and the fluid black. The solid parts have been discretized using 16M tetrahedral cells and a resolution of at least 5 points through the chamber walls. A second-order Galerkin diffusion scheme is applied for spatial discretization and an implicit first-order Euler scheme is used for time integration. While the heat fluxes at the solid boundaries in contact with the fluid are determined from the LES solutions, thermal boundary conditions must be fixed for the solid surfaces that are not in contact with the fluid domain (e.g. external chamber walls, external plenum walls). To do so, the required heat exchange coefficients at the boundaries have been determined through correlations for natural convection on the external side of the chamber and plenum walls. Moreover, Fredrich *et al.* [46] showed that heat losses incurred through radiation can be important. Therefore, to take into account thermal radiation, it is possible to compute an equivalent heat transfer coefficient for the external chamber walls starting from the Stefan-Boltzmann law $\dot{q}_{rad} = \epsilon\sigma T^4$. This procedure yields higher heat transfer coefficients (i.e. h = 100 W/(m^{2}K) with a $\epsilon_{quartz} = 0.8$ for chamber walls and h = 15 W/(m^{2}K) for plenum walls) if compared to only convection [7] and are reported in Fig. 12. This approach neglects the internal wall radiation towards the hot gases, but can be considered as a first order approximation for taking into account radiation heat losses.

The time evolution of the heat release rate and pressure oscillations predicted at the combustion chamber backplane after the thermal convergence is presented in Fig. 13(a). From the unstable phase predicted with the simplified approach in which pressure and heat release rate oscillations were almost in phase satisfying the Rayleigh criterion, a stable condition is recovered when CHT simulations are started. The pressure fluctuations amplitude is of the order of 200 Pa and corresponds to the level observed experimentally (see Fig. 2). Moreover, heat release rate fluctuations seem no more correlated with pressure fluctuations. The spectra computed via Fast-Fourier Transform (FFT) of the stable part of the two signals (i.e., t $\geq$ 0.83 s) are presented in Fig. 13(b) and confirm this observation. No 224 Hz peak appears confirming that the experimentally observed stable condition is recovered. The pressure signal spectrum also shows only a weak 480 Hz peak that does not correlate with heat-release rate fluctuations.

The instantaneous field of solid temperature as computed by AVTP is shown in Fig. 14(a) together with an instantaneous iso-contour of predicted heat-release rate $\dot{q}$ at 10% of maximum value. The temperature of the chamber walls on the internal side reaches a maximum value of around 1350 K at 40 mm from the backplane where the flame is very close to the walls. The temperature goes down when proceeding toward the backplane where the flame is only sporadically present. The backplane has a temperature of around 600K, very similar to the one measured by Yin *et al.* [43] in case $P20_{CB}$. The Biot number being much lower than 1, the temperature at the backplane is more uniform than the one predicted, for example, with the HRT approach in case $P20_{CB}$ (see Fig. 5(a)). The predicted temperature at the centerbody tip instead is notably higher than the one measured in condition $P20_{CB}$ reaching a value of 800 K: even if the thermal power of case $P20_{CB}$ is higher with respect to case $P10$, the equivalence ratio ϕ is also higher in the latter case and yields a higher adiabatic flame temperature. The flame has a V-shape, with a flame-root well attached to the centerbody tip. Figure 14(b) shows the time-averaged temperature $\overline{T}$ and heat-release rate $\overline{\dot{q}}$ in a cut plane with a zoom showing the temperature gradient in the solid and the pre-heating of the gases. The fluid domain is delimited by a white line. The flow reaches 1800 K in the CRZ and downstream of the flame tip where burnt gases are present while the ORZs show lower temperature. The red iso-contour visible close to the centerbody corresponds to a temperature of 450 K and shows the pre-heating of the fresh gases due to the warmed-up solid which is visible also close to

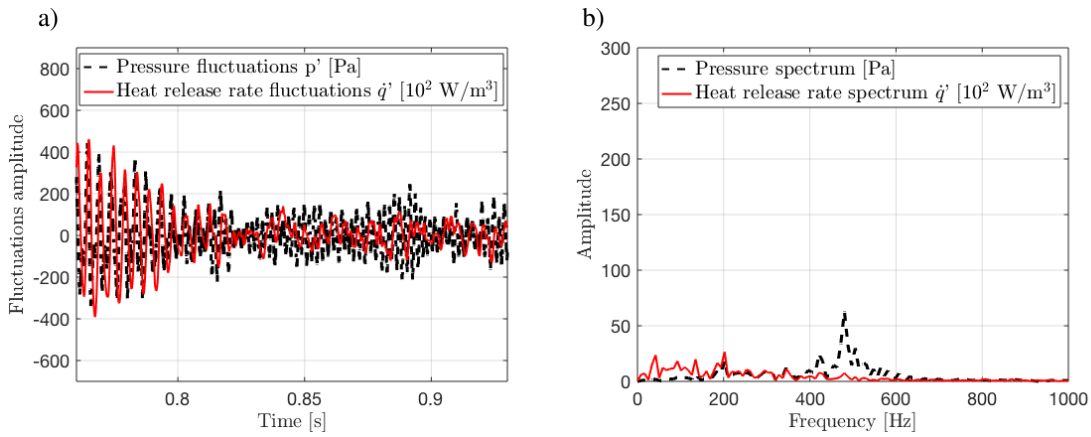

Figure 13: (a) Pressure and heat release rate fluctuations predicted at the combustion chamber backplane. From an unstable phase in which pressure and heat release rate oscillations were almost in phase, satisfying the Rayleigh criterion, a stable condition is recovered with CHT simulations. (b) Spectra of the stable part of the signals, showing that the heat release rate peak at 224 Hz is no more present.

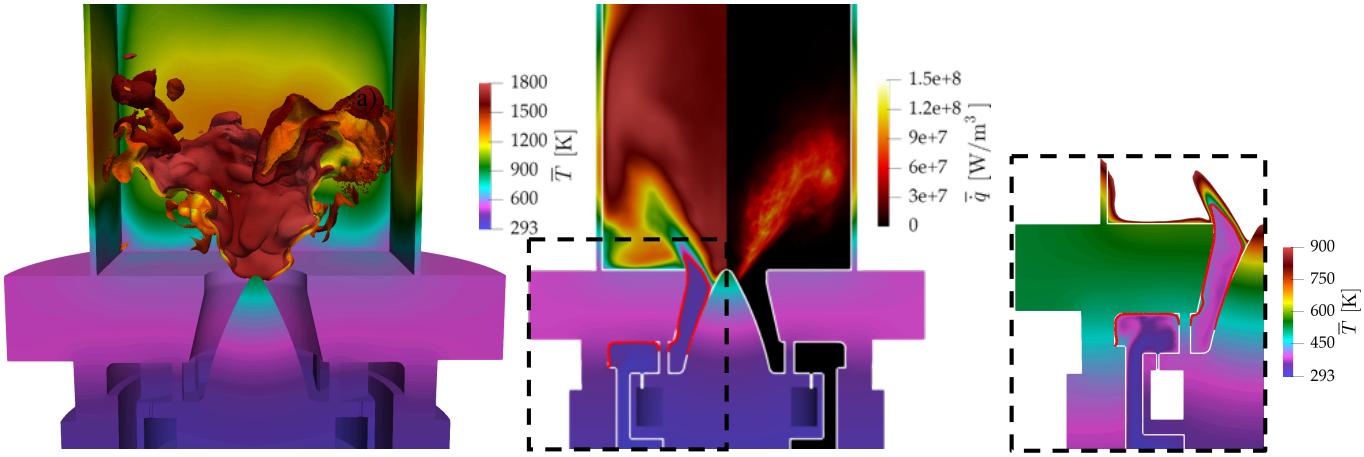

Figure 14: (a) Instantaneous field of solid temperature and iso-contour of heat-release rate $\dot{q}$ at 10% of maximum value; (b) cut-plane showing the time-averaged temperature $\overline{T}$ and heat release rate $\overline{\dot{q}}$ predicted by CHT simulations. The added red iso-contour line corresponds to a temperature of 450 K, showing the pre-heating of the fresh gases by the solid walls. A zoom showing the temperature field with a different colorbar helps visualize the pre-heating of the gases and the temperature gradient in the solid. The fluid domain is delimited by a white line to visualize the separation between solid and fluid parts.

the fuel injection tubes. This is an important feature captured by the CHT simulations, since, as discussed, in previous studies a fresh gas temperature of 320 K has been usually considered, while in this case we observe a pre-heating temperature which is closer to 400 K (starting from a T_{inlet}=293K). Note that the temperature profile of the fresh gases is not homogeneous but reaches higher values close to the walls. The time-average of the predicted heat-release rate $\overline{\dot{q}}$ confirms the V-shape of the flame and shows that the chamber walls are notably hotter in the region where the flame tips reach the walls. No flame is predicted in the CRZ while in the ORZ weaker heat release rate can be noticed.

Finally, the CHT simulations are compared to experimental data in Fig. 15. Experimental normalized time-averaged LOS OH* chemiluminescence image (which is a qualitative indicator for the heat release rate for lean premixed flames) and LOS field of predicted heat release rate $\overline{\dot{q}}$ are shown in Fig. 15(a). The length and flame angle are retrieved by the CHT simulations and a better agreement is achieved with respect to the simplified approach (see Fig. 8). LES is also able to predict the high region of heat release rate in the top central part of the flame while low intensity is predicted in the CRZ, just downstream of the centerbody. The flame tip shape is correctly predicted together with the distance from the external chamber walls. Figure 15(b) presents the comparison of the experimental normalized time-averaged OH-PLIF signal with the predicted OH mass fraction $\overline{Y_{OH}}$. CHT simulations agree with the experimental data, both in terms of flame length and angle. The flame tip reaches a height of 50 mm from the backplane while low OH mass fraction intensity is predicted in the ORZ. As in experiments, LES predicts no OH mass fraction $\overline{Y_{OH}}$ in the high velocity region of the swirled flow. Experimental and numerical time-averaged velocity field in the plane $\overline{\vec{v}_{//}}$ are indicated by arrows that are tangential to the velocity vector and whose length and color indicate the velocity magnitude. Both in LES and experiments, a high velocity region (i.e. white arrows) is predicted at the exit of the swirler. A CRZ is also visible together with the ORZ where the velocity in the plane is very weak.

A more quantitative validation of the CHT simulations can be

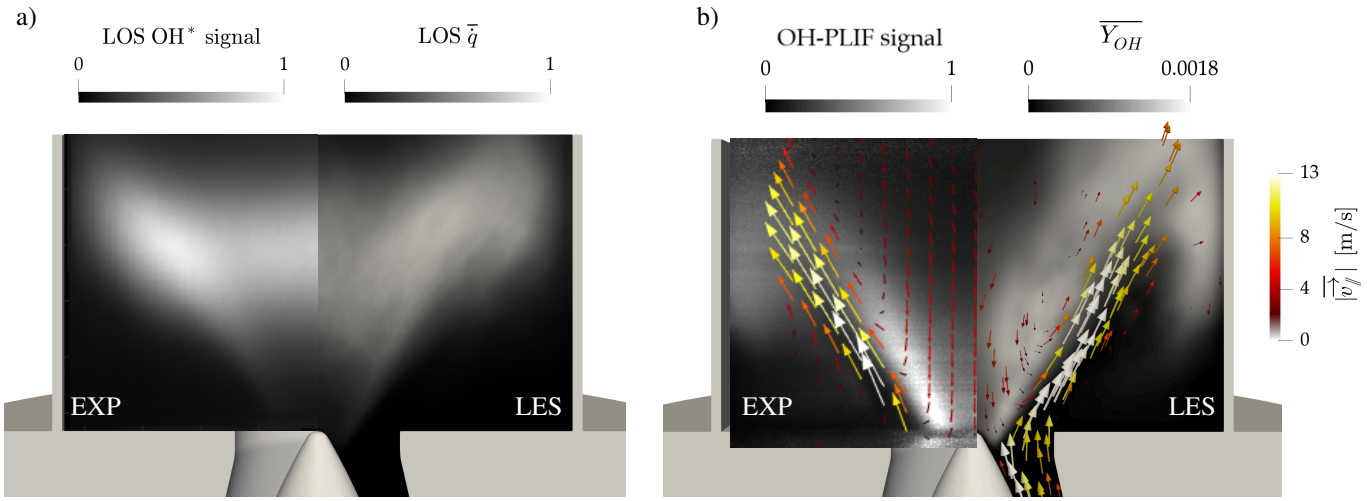

Figure 15: Validation of CHT simulations: (a) Comparison of experimental normalized time-averaged Line of Sight (LOS) OH* chemiluminescence image with LOS predicted heat release rate $\bar{\dot{q}}$; (b) Comparison of experimental normalized time-averaged OH-PLIF signal with predicted OH mass fraction $\overline{Y_{OH}}$. The arrows are tangential to the experimental and numerical time-averaged velocity field in the plane $\overrightarrow{v_{//}}$. Their length and color indicate the velocity magnitude.

assessed by comparing the experimentally measured mean and rms profiles of velocity components at different measurement planes downstream of the backplane with the predicted profiles: LES captures the mean axial velocity component (Fig. 16(a)), both in terms of magnitude and opening of the swirled flow. The magnitude of the CRZ is slightly underestimated at h = 15 mm and 20 mm from the chamber backplane but a good match is retrieved at h = 30 mm. RMS oscillations are instead slightly over-estimated (Fig. 17(a)). This mismatch may be explained by uncertainties of the experimental values and the small absolute magnitude of the RMS. Mean and rms of both radial and tangential velocity are captured by LES as shown in Fig. 16(b-c) and Fig. 17(b-c), respectively. The poorer match for tangential velocity profiles may be due to PIV measurement uncertainties for which errors in the out-of-plane direction (in this case, the tangential) are typically higher than for the in-plane velocity components. [75].

3.3. Heat transfer impact on thermoacoustic driving mechanisms

The previous sections have shown that the correct stable thermoacoustic behavior of the flame was predicted only with CHT simulations and not with HRT. We analyze now the impact of heat transfer on the instability-driving mechanisms starting with acoustic modes structures.

Figure 18(a) shows the relative mean temperature difference between the CHT and the HRT simulations in the middle plane of the combustor with the white iso-contours indicating zero values. The combustion chamber has a slightly lower mean temperature in CHT while the ORZs present significantly lower temperature (dark blue zones). On the contrary, a strong preheating is observed in the swirler and close to the centerbody walls (red zones). At the same time, the flow in the plenum is slightly warmed while the flow at the air inlet is cooler since in CHT T_{inlet} is fixed at the ambient temperature (293K). This highlights the main differences between the HRT and the CHT approaches: the HRT method is not able to capture the detailed temperature variation at the walls since it also depends on the heat re-distribution due to conduction in the transverse direction. Likewise, the unsteady heat transfer between the flow and the solid is a function of the relative flame position with respect to the walls which in turn is dependent on the non-homogeneous and unsteady preheating of the gases.[6]

The corresponding time-averaged sound speed $\bar{c}$ are compared in Figs. 18(b-c): a globally lower sound speed value is achieved with CHT in the chamber with the most significant differences observed in the ORZs are probably due to the fact that the flame does not oscillate anymore and no heat release rate happens in these regions. Finally, another difference can be noted along the chamber walls: for HRT, the zones where the flame tips reach the wall are very hot, while for CHT, the temperature field, and hence the sound speed, close to the chamber walls are more homogeneous due to the heat conduction in the solid.

The two mean fields shown in Fig.18(b-c) are used to compute the first two acoustic modes of the system using the Helmholtz solver AVSP [76] giving comparable results in terms of both modes frequency and shapes. The first mode is predicted at a frequency of 257 Hz. Modulus and phase data (Fig. 19(a-b)) suggest that this 257 Hz mode is the 1/4 wave (or bulk) mode of the system: the amplitude of the pressure oscillation $|\ p'\ |$ is larger in the plenum (Fig. 19(a)) and the chamber as well as the plenum oscillate in phase (Fig. 19(b)). The limit cycle frequency predicted by the HRT method is 224 Hz, close to the 1/4 wave mode frequency, suggesting that the flame with HRT boundary conditions couples with this first mode (see

[6]Note that even in the unrealistic scenario in which a local tuning of R were possible, HRT would however miss the non-homogeneous preheating of the gases. More generally, the HRT approach cannot reproduce all the situations in which the solid provides energy to the gases (e.g. bluff-body, plenum): since the reference temperature in HRT is fixed at 293 K it is always the gas that provides energy to the solid. Changing T_{ref} locally means introducing additional unknowns while also losing the possibility to apply tuned values of R for all different operating conditions.

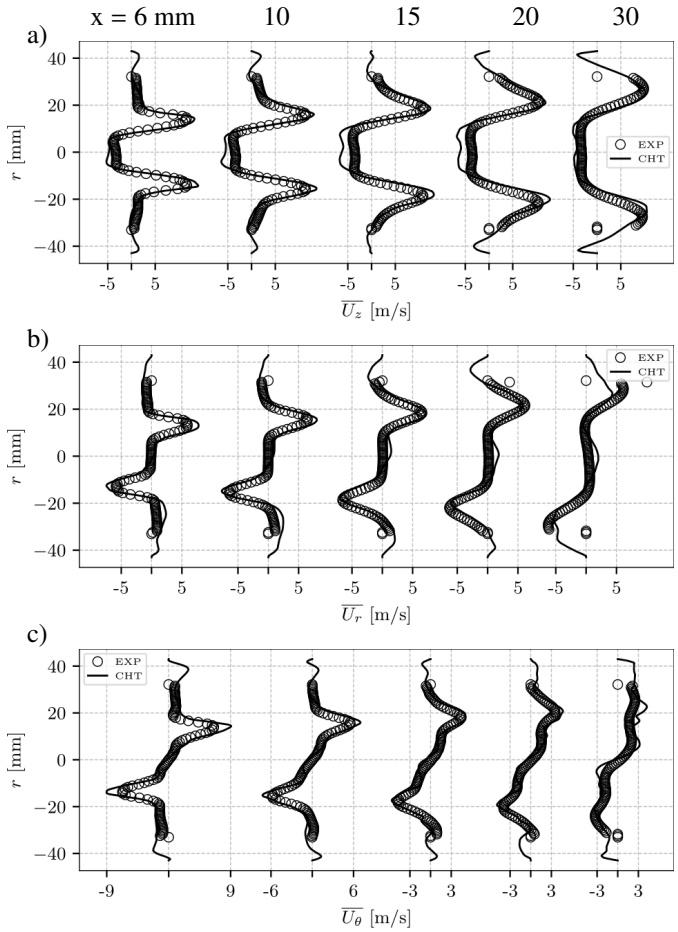

Figure 16: Profiles of Mean (a) axial velocity, (b) radial velocity and (c) tangential velocity at measurement planes at x = 6, 10, 15, 20 and 30 mm downstream of the combustion chamber backplane for the CHT simulations in comparison to experiments.

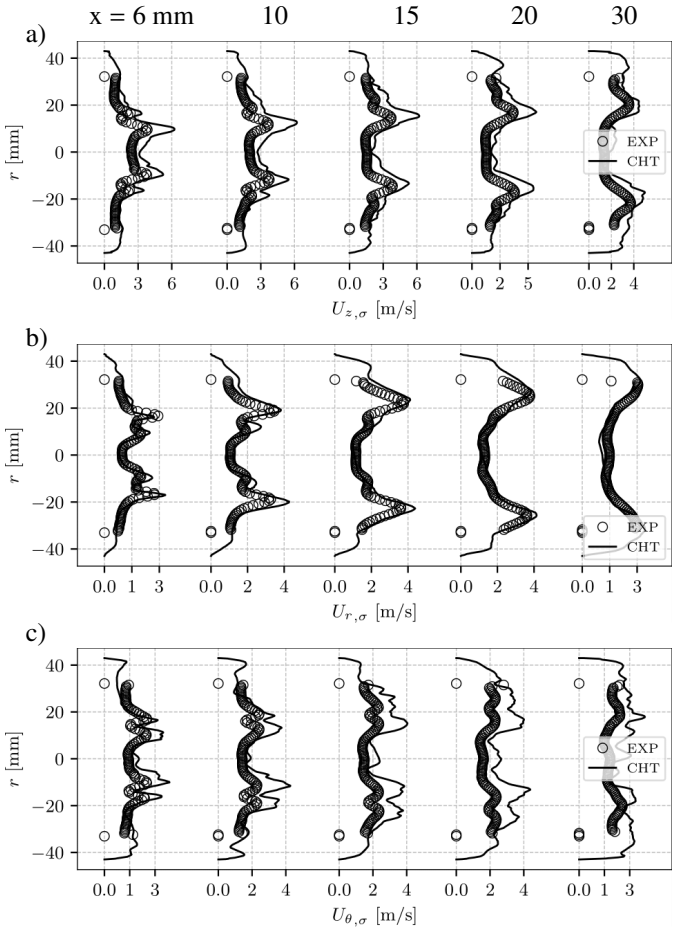

Figure 17: Profiles of RMS (a) axial velocity, (b) radial velocity and (c) tangential velocity at measurement planes at x = 6, 10, 15, 20 and 30 mm downstream of the combustion chamber backplane for the CHT simulations in comparison to experiments.

Fig. 9). The amplitude and phase of the second acoustic mode at 480 Hz are shown in Fig. 19(c) and Fig. 19(d), respectively. It corresponds to a 3/4 wave mode: a pressure antinode is found in the combustion chamber and the two volumes of the system (chamber and plenum) oscillate in phase opposition. Traces of this mode are also visible in the LES simulations (Fig. 9 and Fig. 13) matches this frequency. The flame does not couple with this mode during the limit cycle predicted by the HRT approach. Note also that the frequencies of the predicted acoustic modes match the two small peaks observable in the experimental pressure signal (Fig. 2). This analysis confirms that heat transfer does not change the system acoustics significantly.

The flame response was also investigated using Dynamic Mode Decomposition [77] (DMD) to reconstruct the oscillating modes of the system and extract the response of pressure, velocity components, heat release rate and equivalence ratio at the limit cycle frequency of 224 Hz [78]. The DMD input is 400 instantaneous 3D LES fields. Once the DMD mode has been computed at the frequency of interest, it is possible to investigate the coherent spatial features of each variable by comparing its phase with respect to a reference variable, in the present study pressure. If one selects the heat release rate as the variable of interest and computes the phase difference with respect to the pressure DMD mode, a three-dimensional Rayleigh index field is retrieved as $\mathcal{R}e(\widehat{RI}) = \mathcal{T}_{q,p} = |\hat{p}||\hat{q}|\cos\left(\varphi_q - \varphi_p\right)$ [79, 80]. An equivalence ratio - pressure fluctuations correlation index can be defined as $\mathcal{T}_{\phi,p} = |\hat{p}||\hat{\phi}|\cos\left(\varphi_\phi - \varphi_p\right)$ indicating whether fluctuations of equivalence ratio ϕ are contributing positively or negatively to pressure oscillations and hence to thermoacoustic instability.

The normalized real part of the Rayleigh index $\mathcal{R}e(\widehat{RI})$ and the normalized equivalence ratio - pressure fluctuations correlation index $\mathcal{T}_{\phi,p}$ for the unstable flame predicted by LES with the HRT approach are presented in Fig. 20(a). As expected, the Rayleigh index $\mathcal{R}e(\widehat{RI})$ presents large zones (colored in red) in which the flame oscillates in phase and drive pressure fluctuations. This mainly happens at the flame root near the centerbody and at the flame branches (10 mm < x < 40 mm). On the contrary, downstream of the centerbody, negative values (colored in blue) of Rayleigh index $\mathcal{R}e(\widehat{RI})$ are visible: when the flame detaches from the centerbody (Fig. 10(d)) it damps pressure oscillations. The flame tips (for x > 40 mm) also show slight negative values of $\mathcal{R}e(\widehat{RI})$. The instability is supported by equivalence ratio fluctuations as underlined by the equivalence

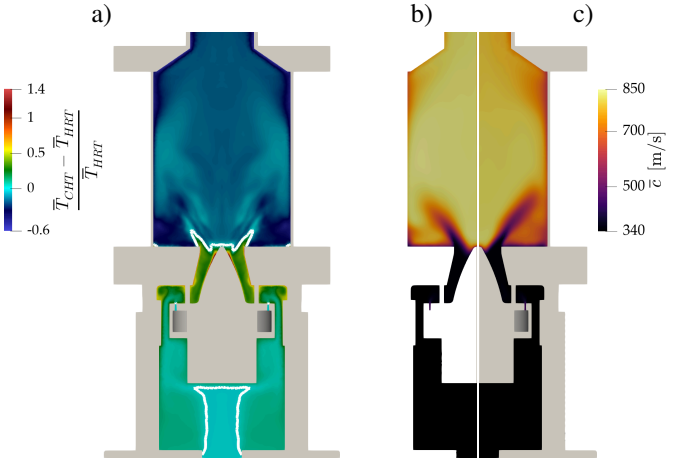

Figure 18: (a) Relative mean temperature difference between the CHT and the HRT approaches on the middle plane of the combustor with white iso-contours corresponding to zero values. Predicted time-averaged sound speed $\overline{c}$ field in (b) HRT-LES and (c) CHT-LES.

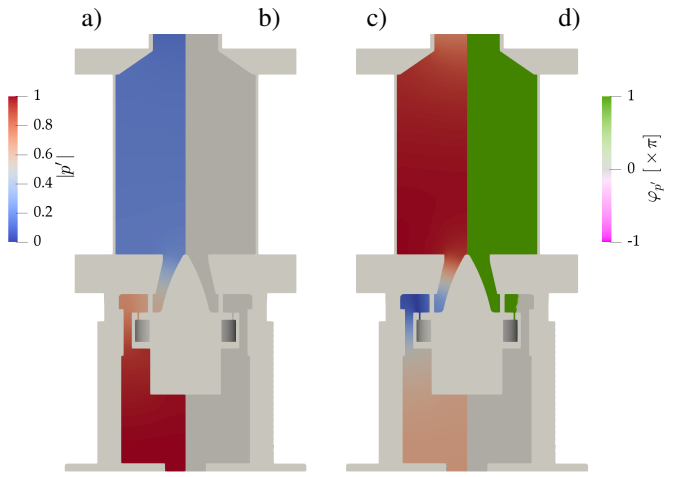

Figure 19: Acoustic modes computed with the Helmholtz solver. Both modelling approaches result in similar modes. (a) Amplitude and (b) phase of the first acoustic (plenum) mode at 257 Hz. (c) Amplitude and (d) phase of the second acoustic (chamber) mode at 480 Hz.

ratio - pressure fluctuations correlation index $\mathcal{T}_{\phi,p}$: regions just upstream of the flame root (near the centerbody) show a positive (colored in green) correlation index $\mathcal{T}_{\phi,p}$, indicating that the equivalence ratio fluctuations are in phase with the acoustic oscillations. These equivalence ratio oscillations are supported by the flapping of the jet: since the first acoustic mode is a 1/4 wave mode (Fig. 19) where chamber and plenum oscillate in phase, it is straightforward to visualize the rich gas pocket periodically released in the combustion chamber corresponding to the green regions upstream the flame root at x = 0 mm. At the beginning, the correlation index $\mathcal{T}_{\phi,p}$ is green at the fuel tube exits: when pressure is increasing, the equivalence ratio is increasing in this region too (i.e. CH_4 is accumulated). Moving further downstream, when fuel pockets are convected to the middle of the centerbody, half a thermoacoustic cycle has passed and pressure is decreasing: therefore, these regions are flagged in purple (i.e. negative contributions) since when the pockets reach this zone locally increasing the equivalence ratio, pressure is decreasing. Finally, after one thermoacoustic cycle, the fuel pockets reach the flame-root and their contribution is again positive. This analysis confirms that rich gas pockets being periodically pushed into the chamber are feeding the thermoacoustic oscillation.

A different situation results from the DMD analysis when switching from the HRT to the CHT approach (i.e. for t < 0.8 s in Fig. 13(a)). The normalized real part of the Rayleigh index $\mathcal{R}e(\widehat{RI})$ and the normalized equivalence ratio - pressure fluctuations correlation index $\mathcal{T}_{\phi,p}$ computed during this transient phase are showed in Fig. 20(b). The flapping of the fuel jet is still present and the rich gas pocket periodically released in the combustion chamber can be identified by the green spots of $\mathcal{T}_{\phi,p}$. The $\mathcal{R}e(\widehat{RI})$ at the flame root resembles the one of the HRT unstable flame (Fig. 20(a)): the heat release rate fluctuations in this region are in phase with the pressure oscillations still present in this transition phase. Contrarily, the flame branches (10 mm < x < 40 mm) show lower positive values of $\mathcal{R}e(\widehat{RI})$ and a less coherent spatial distribution with respect to the unstable HRT flame (Fig. 20(a)). The flame tips (x > 40 mm) present marked zones of negative $\mathcal{R}e(\widehat{RI})$, indicating that these regions are contributing negatively to the thermoacoustic oscillations.

Finally, the normalized real part of the Rayleigh index $\mathcal{R}e(\widehat{RI})$ and the normalized equivalence ratio - pressure fluctuations correlation index $\mathcal{T}_{\phi,p}$ for the CHT stable flame are presented in Fig. 20(c). As expected in a thermoacoustically stable condition, the Rayleigh index $\mathcal{R}e(\widehat{RI})$ and the correlation index $\mathcal{T}_{\phi,p}$ fields do not show any coherent spatial distribution at the selected frequency.

The three Rayleigh index $\mathcal{R}e(\widehat{RI})$ maps shown in Fig. 20 can also be integrated over the combustor cross section S_c to obtain the one-dimensional mean axial distributions:

$$\langle \mathcal{R}e(\widehat{RI}) \rangle(x) = \frac{1}{S_c} \iint_{S_c} \mathcal{R}e(\widehat{RI})(x,y,z) dydz. \qquad (3)$$

A similar treatment is performed for the two mean heat release rate ($\langle \overline{\dot{q}} \rangle$) fields predicted with HRT (Fig. 8) and CHT (Fig. 15(a)).

The axial evolution of these quantities normalized with respect to their respective maximum value are plotted in Fig. 21. As already discussed, the flame with HRT is more compact with the peak of mean heat release rate at x = 27 mm (black line with circular mark). A more elongated distribution is instead observed with CHT (gray line with circular mark) where $\langle \overline{\dot{q}} \rangle$ peaks further downstream at x = 35 mm. The axial distributions of $\langle \mathcal{R}e(\widehat{RI}) \rangle$ are consistent with Fig. 20. In the HRT case (black line) a significant positive contribution is present at the flame root (x < 10 mm) while the largest positive contribution is related to the central part of the flame branches (20 mm < x < 35 mm) just downstream of the maximum peak of $\langle \overline{\dot{q}} \rangle$. The flame tips (x > 40 mm) show instead a significant negative contribution that is not sufficient to stabilize the flame. The axial distribution of the Rayleigh index $\langle \mathcal{R}e(\widehat{RI}) \rangle$ for CHT is almost zero as expected for a thermoacoustically stable case (gray line). It is also interesting to plot the Rayleigh index $\langle \mathcal{R}e(\widehat{RI}) \rangle$ axial distribution during the transient stabilization process when switching

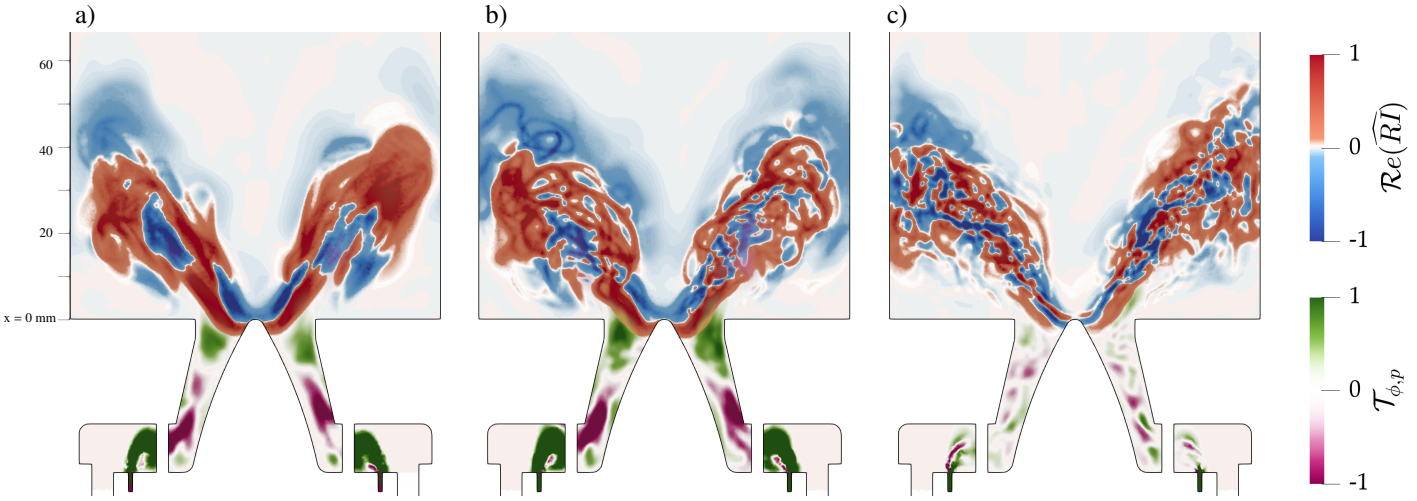

Figure 20: Cut-plane showing the Dynamic Mode Decomposition (DMD) at 224 Hz. Normalized real part of the Rayleigh index formulation in frequency domain $\mathcal{R}e(\widehat{RI})$ and normalized equivalence ratio - pressure fluctuations correlation index $\mathcal{T}_{\phi,p}$ for (a) the unstable flame predicted by LES with HRT approach, (b) the transient stabilization phase when switching to CHT and (c) the stable flame predicted by CHT.

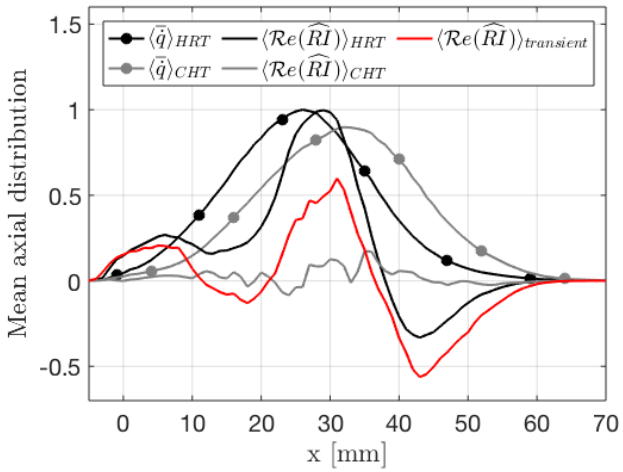

Figure 21: Mean axial distributions of normalized mean heat release rate $\langle\bar{\dot{q}}\rangle$ and DMD Rayleigh index $\langle\mathcal{R}e(\widehat{RI})\rangle$ for HRT (black) and CHT (gray) approaches. The Rayleigh index $\langle\mathcal{R}e(\widehat{RI})\rangle$ during the transient stabilization process (red) when switching to CHT is also showed.

to CHT (red line). While the $\langle\mathcal{R}e(\widehat{RI})\rangle$ field at the flame root (x < 10 mm) is similar to the one of the HRT unstable flame (black curve), flame branches show a lower positive contribution (10 mm < x < 40 mm) and flame tips (x > 40 mm) show larger negative values: when switching to CHT simulations, the stabilization process starts at the flame branches and tips that are in contact with the combustion chamber walls. The instability-driving regions at the central part of the flame branches become less pronounced and the flame tips negative contributions to the thermoaoustic oscillation are enhanced, hence promoting the flame stabilization. The main difference in the heat transfer at the chamber walls between HRT and CHT is the rapid distribution of heat from hot regions where the flame reaches the walls: the latter can be predicted only by CHT simulations in which heat conduction through the solid is correctly taken into account.

4. Conclusions

The impact of wall heat transfer treatments on the numerical prediction of the thermoacoustic behavior of the PRECCINSTA test bench was studied. First, a simplified approach (HRT) to specify thermal boundary condition based on the prescription of the thermal resistances tuned from experimental measurements is proposed. This approach provides satisfactory global agreement with experimental data in terms of mean flame shape but nonphysical unsteady dynamics: the LES flame exhibits a thermoacoustic oscillation which is not observed experimentally. This oscillation can not be suppressed by changing the acoustic impedance of the air or fuel inlets. However, going to full Conjugate Heat Transfer (CHT) simulations, the flame becomes stable, confirming the strong impact of heat transfer on the predictions of the present configuration.

No relevant difference between HRT and CHT cases is observed when comparing the sound speed fields or the system acoustic modes obtained with a Helmholtz solver: the acoustic properties of the system are captured correctly with both approaches. Dynamic Mode Decomposition (DMD) reveals that the instabilities of the HRT LES are coupled to a flapping motion of the fuel jets: the flame responds to these perturbations in phase with the acoustic pressure sustaining the thermoacoustic modes. On the contrary, for CHT simulations, the dynamics of the flame branches is slightly but sufficiently altered to modify the flame response, leading to the stabilization of the system.

To conclude, the correct prediction of wall heat transfer appears important to capture the experimental thermoacoustic behaviour of the PRECCINSTA combustor. More generally, this confirms that high fidelity can be achieved for combustion LES solvers only when precise boundary conditions are used not only for the inflow and outflow acoustic impedances but also for the wall thermal boundary conditions.

Acknowledgements and Fundings

This project has received funding from the H2020-MSC-ITN Grant Agreement No 766264 (MAGISTER), the MSCA Grant Agreement No 843958 (CLEANERFLAMES - D. Laera Individual Fellowship), the H2020 Grant Agreement 952181 (COEC - Center of Excellence in Combustion) and the ERC H2020 Grant Agreement 682383. HPC resources from GENCI (Grant 2021-A0092B10157) and the PRACE Projects 2020225434 (FANTASTIC-H2) and 2020225436 (REVOLUTION) are also acknowledged. The authors gratefully acknowledge the assistance of Dr. Ianko Chterev in acquiring the measurements for the test case referred to as $P10$ and Dr. Wolfgang Meier from the German Aerospace Center (DLR) for providing the experimental data for the test case $P30_W$. The authors would also like to thank Dr. Stephane Richard from Safran Helicopter Engines (SHE) for valuable discussions and Dr. Florent Duchaine from CERFACS for support on the AVTP solver.

Appendix A. Operating procedure and correlations for implementing the HRT method

This appendix illustrates the operating procedure and some useful correlations for implementing the HRT method. Indeed, whether or not temperature experimental data are available, a good guess for the thermal resistances can be set for each surface as an equivalent resistance R_{eq}, similarly to an electric circuit, assuming that radiation and convection act in parallel.

$$R_{eq} = R_{cond} + \frac{1}{1/R_{conv} + 1/R_{rad}}. \tag{A.1}$$

To compute the different resistances, the following equations can be used:

$$R_{cond} = L_s/\lambda_s, \tag{A.2}$$

$$\frac{1}{R_{conv}} = h_{conv} = \frac{\lambda_{air}}{L_{conv}}\left(0.68 + \frac{0.67\mathrm{Ra}_L^{1/4}}{(1+(0.492/\mathrm{Pr})^{9/16})^{4/9}}\right), \tag{A.3}$$

$$R_{rad} = \epsilon\sigma\frac{T_{wall}^4 - T_{ambient}^4}{T_{wall} - T_{ambient}}. \tag{A.4}$$

where L_s is the characteristic length of the conduction problem (e.g. thickness of the wall), λ_s the solid thermal conductivity, L_{cv} the characteristic length of the convection problem (e.g. length of the wall), Ra_L the Rayleigh number based on the characteristic length L, Pr the Prandtl number, ϵ the emissivity and σ the Stefan–Boltzmann constant. Note that Eq. A.3 is valid for natural convection from a vertical plate and for $10^{-1} < \mathrm{Ra}_L < 10^9$ but standard correlations are available in literature for other flow conditions [63, 64]. It is also worth underlining that in Eq. A.3 the flow properties have to be determined for an average temperature $\mathrm{T}_{flow} = (\mathrm{T}_{ambient} + \mathrm{T}_{wall})/2$ and hence requires the estimation of T_{wall}. The same applies for Eq. A.4.

When temperature experimental data are not available, the depicted methodology can give reasonable values for the thermal resistances and avoid the use of adiabatic conditions. However, if experimental data are available, a tuning procedure can be performed starting from these initial values.

In the present study, the initial values for the centerbody and backplane have been calculated neglecting convection and radiation (i.e. the temperature of the solid was expected to be low) and considering a characterictic length L_s = 36 mm (i.e. the height of the bluff-body) and a thermal conductivity λ_s = 15 W/m K. This results in a $\mathrm{R}_{initial} = 2.4\times10^{-3}$ m^{2}K/W. For the chamber walls instead, T_{wall} is assumed to be close to 1200 K: radiation cannot be neglected. A value of $\epsilon_{quartz} = 0.8$ is assumed to compute the R_{rad}. R_{conv} is determined assuming a characteristic length L_{cv} = 114 mm (i.e. height of the chamber walls), a $\mathrm{Ra}_L = 5.8\times10^6$ and a Pr = 0.7. $\mathrm{R}_{conduction}$ is computed taking into account the 1.7 mm thickness of the walls and the λ_s = 1.4 W/m K. The resulting equivalent $\mathrm{R}_{eq,\ initial} = 1\times10^{-2}$ m^{2}K/W. Note that these values have the same order of magnitude of the values found after the tuning procedure (Sec. 3.1), verifying the assumptions.

To perform the iterative tuning procedure, a linearization of the thermal problem was used. The heat flux Φ_q at the wall can be determined as follows:

$$\Phi_{q,\ initial} = \frac{T_{wall} - T_{ref}}{R_{eq,\ initial}} = \frac{T_{flow} - T_{wall}}{R_{flow}} \tag{A.5}$$

where T_{flow} is the temperature of the flow inside the combustion chamber near the wall (out of the thermal boundary layer) and R_{flow} is the corresponding convection resistance. Performing the first LES with $\mathrm{R}_{eq,\ initial}$ one finds the unknown variables T_{wall}, T_{flow} and R_{flow}. At this point, we can assume, as a first approximation, that the variation of R_{flow} (and hence the thermal boundary layer) with T_{wall} is negligible. Therefore, if we impose the $\mathrm{T}_{wall,\ exp}$ in Eq. we can compute $\mathrm{R}_{eq,\ step1}$:

$$\Phi_{q,\ step1} = \frac{T_{wall,\ exp} - T_{ref}}{R_{eq,\ step1}} = \frac{T_{flow} - T_{wall,\ exp}}{R_{flow}}, \tag{A.6}$$

$$R_{eq,\ step1} = \frac{T_{wall,\ exp} - T_{ref}}{T_{flow} - T_{wall,\ exp}} R_{flow}. \tag{A.7}$$

LES is then performed with the new value of $\mathrm{R}_{eq,\ step1}$ and a new estimation of T_{wall} is produced. If the latter is sufficiently close to $\mathrm{T}_{wall,\ exp}$ the tuning procedure is completed, otherwise a new iteration is performed. In the present study, starting from reasonable values for the resistances, a single iteration was needed to reach satisfactory agreement with $\mathrm{T}_{wall,exp}$.

References

[1] S. Roux, G. Lartigue, T. Poinsot, U. Meier, C. Bérat, Studies of mean and unsteady flow in a swirled combustor using experiments, acoustic analysis, and large eddy simulations, Combust. Flame 141 (2005) 40–54.

[2] V. Moureau, P. Domingo, L. Vervisch, From large-eddy simulation to direct numerical simulation of a lean premixed swirl flame: Filtered laminar flame-pdf modeling, Combust. Flame 158 (2011) 1340–1357.

[3] Y. Huang, H.-G. Sung, S.-Y. Hsieh, V. Yang, Large-eddy simulation of combustion dynamics of lean-premixed swirl-stabilized combustor, J. Propul. Power 19 (2003) 782–794.
[4] P. W. Agostinelli, Y. H. Kwah, S. Richard, G. Exilard, J. R. Dawson, L. Gicquel, T. Poinsot, Numerical and experimental flame stabilization analysis in the new spinning combustion technology framework, ASME Turbo Expo 2020, Paper No. GT2020-15035, p. V04AT04A058 (13 pages).
[5] L. Y. Gicquel, G. Staffelbach, T. Poinsot, Large eddy simulations of gaseous flames in gas turbine combustion chambers, Prog. Energ. Combust. 38 (2012) 782–817.
[6] E. Lo Schiavo, D. Laera, E. Riber, L. Gicquel, T. Poinsot, Effects of liquid fuel/wall interaction on thermoacoustic instabilities in swirling spray flames, Combust. Flame 219 (2020) 86–101.
[7] C. Kraus, L. Selle, T. Poinsot, Coupling heat transfer and large eddy simulation for combustion instability prediction in a swirl burner, Combust. Flame 191 (2018) 239–251.
[8] T. F. Guiberti, D. Durox, P. Scouflaire, T. Schuller, Impact of heat loss and hydrogen enrichment on the shape of confined swirling flames, Proc. Combust. Inst. 35 (2015) 1385–1392.
[9] L. Tay Wo Chong, T. Komarek, M. Zellhuber, J. Lenz, C. Hirsch, W. Polifke, Influence of Strain and Heat loss on Flame Stabilization in a Non-Adiabatic Combustor, Proceedings of European Combustion Meeting (2009) 1–6.
[10] P. Zhao, L. Wang, N. Chakraborty, Analysis of the flame-wall interaction in premixed turbulent combustion, J. Fluid Mech. 848 (2018) 193–218.
[11] F. N. Egolfopoulos, H. Zhang, Z. Zhang, Wall effects on the propagation and extinction of steady, strained, laminar premixed flames, Combust. Flame 109 (1997) 237–252.
[12] F. Duchaine, F. Boudy, D. Durox, T. Poinsot, Sensitivity analysis of transfer functions of laminar flames, Combust. Flame 158 (2011) 2384–2394.
[13] T. Poinsot, Prediction and control of combustion instabilities in real engines, Proc. Combust. Inst. 36 (2017) 1–28.
[14] W. Polifke, Modeling and analysis of premixed flame dynamics by means of distributed time delays, Prog. Energy Combust. Sci. 79 (2020) 100845.
[15] T. Schuller, T. Poinsot, S. Candel, Dynamics and control of premixed combustion systems based on flame transfer and describing functions, J. Fluid Mech. 894 (2020) P1.
[16] D. Mejia, L. Selle, R. Bazile, T. Poinsot, Wall-temperature effects on flame response to acoustic oscillations, Proc. Combust. Inst. 35 (2015) 3201–3208.
[17] K. S. Kedia, H. M. Altay, A. F. Ghoniem, Impact of flame-wall interaction on premixed flame dynamics and transfer function characteristics, Proc. Combust. Inst. 33 (2011) 1113–1120.
[18] S. Hong, S. J. Shanbhogue, K. S. Kedia, A. F. Ghoniem, Impact of the flame-holder heat-transfer characteristics on the onset of combustion instability, Combust. Sci. Technol. 185 (2013) 1541–1567.
[19] A. Cuquel, D. Durox, T. Schuller, Impact of flame base dynamics on the non-linear frequency response of conical flames, Comptes Rendus Mécanique 341 (2013) 171–180.
[20] M. Lohrmann, H. Büchner, Prediction of stability limits for lp and lpp gas turbine combustors, Combust. Sci. Technol. 177 (2005) 2243–2273.
[21] R. Heydarlaki, W. Aitchison, P. Kostka, S. Kheirkhah, Influences of initial and transient combustor wall-temperature on thermoacoustic oscillations of a small-scale power generator, Exp. Therm. Fluid Sci. 109 (2019) 109856.
[22] S. Berger, F. Duchaine, L. Y. M. Gicquel, Bluff-body Thermal Property and Initial State Effects on a Laminar Premixed Flame Anchoring Pattern, Flow, Turbul. Combust. 100 (2018) 561–591.
[23] C. Fureby, Large Eddy Simulation of turbulent reacting flows with conjugate heat transfer and radiative heat transfer, Proc. Combust. Inst. 38 (2021) 3021–3029.
[24] J. C. Massey, Z. X. Chen, N. Swaminathan, Modelling Heat Loss Effects in the Large Eddy Simulation of a Lean Swirl-Stabilised Flame, Flow, Turbul. Combust. 106 (2020) 1355–1378.
[25] R. Kaess, W. Polifke, T. Poinsot, N. Noiray, D. Durox, T. Schuller, S. Candel, Cfd-based mapping of the thermo-acoustic stability of a laminar premix burner, Center for Turbulence Research, Stanford University, 2008, p. 289.
[26] A. Chatelier, T. Guiberti, R. Mercier, N. Bertier, B. Fiorina, T. Schuller, Experimental and Numerical Investigation of the Response of a Swirled Flame to Flow Modulations in a Non-Adiabatic Combustor, Flow, Turbul. Combust. 102 (2019) 995–1023.
[27] Y. Huang, H. G. Sung, S. Y. Hsieh, V. Yang, Large-Eddy Simulation of Combustion Dynamics of Lean-Premixed Swirl-Stabilized Combustor, J. Propuls. Power 19 (2003) 782–794.
[28] P. Bénard, G. Lartigue, V. Moureau, R. Mercier, Large-eddy simulation of the lean-premixed preccinsta burner with wall heat loss, Proc. Combust. Inst. 37 (2019) 5233–5243.
[29] X. Han, D. Laera, A. S. Morgans, C. J. Sung, X. Hui, Y. Z. Lin, Flame macrostructures and thermoacoustic instabilities in stratified swirling flames, Proc. Combust. Inst. 37 (2019) 5377–5384.
[30] X. Han, D. Laera, D. Yang, C. Zhang, J. Wang, X. Hui, Y. Lin, A. Morgans, C.-J. Sung, Flame interactions in a stratified swirl burner: Flame stabilization, combustion instabilities and beating oscillations, Combust. Flame 212 (2020) 500 – 509.
[31] H. G. Li, P. Khare, H. G. Sung, V. Yang, A Large-Eddy-Simulation Study of Combustion Dynamics of Bluff-Body Stabilized Flames, Combust. Sci. Technol. 188 (2016) 924–952.
[32] A. Ghani, T. Poinsot, L. Gicquel, G. Staffelbach, LES of longitudinal and transverse self-excited combustion instabilities in a bluff-body stabilized turbulent premixed flame, Combust. Flame 162 (2015) 4075–4083.
[33] P. Wolf, G. Staffelbach, L. Y. Gicquel, J.-D. Müller, T. Poinsot, Acoustic and Large Eddy Simulation studies of azimuthal modes in annular combustion chambers, Combust. Flame 159 (2012) 3398–3413.
[34] A. Urbano, L. Selle, G. Staffelbach, B. Cuenot, T. Schmitt, S. Ducruix, S. Candel, Exploration of combustion instability triggering using Large Eddy Simulation of a multiple injector liquid rocket engine, Combust. Flame 169 (2016) 129–140.
[35] M. Shahi, J. B. Kok, J. C. Roman Casado, A. K. Pozarlik, Transient heat transfer between a turbulent lean partially premixed flame in limit cycle oscillation and the walls of a can type combustor, Appl. Therm. Eng. 81 (2015) 128–139.
[36] S. R. Gubba, S. S. Ibrahim, W. Malalasekera, A. R. Masri, Measurements and LES calculations of turbulent premixed flame propagation past repeated obstacles, Combust. Flame 158 (2011) 2465–2481.
[37] S. Gövert, D. Mira, J. B. Kok, M. Vázquez, G. Houzeaux, Turbulent combustion modelling of a confined premixed jet flame including heat loss effects using tabulated chemistry, Appl. Energy 156 (2015) 804–815.
[38] D. Laera, P. W. Agostinelli, L. Selle, Q. Cazères, G. Oztarlik, T. Schuller, L. Gicquel, T. Poinsot, Stabilization mechanisms of CH4 premixed swirled flame enriched with a non-premixed hydrogen injection, Proc. Combust. Inst. 38 (2021) 6355–6363.
[39] S. Berger, S. Richard, F. Duchaine, G. Staffelbach, L. Y. Gicquel, On the sensitivity of a helicopter combustor wall temperature to convective and radiative thermal loads, Appl. Therm. Eng. 103 (2016) 1450–1459.
[40] W. Meier, P. Weigand, X. Duan, R. Giezendanner-Thoben, Detailed characterization of the dynamics of thermoacoustic pulsations in a lean premixed swirl flame, Combust. Flame 150 (2007) 2–26.
[41] P. Weigand, X. Duan, W. Meier, U. Meier, M. Aigner, C. Bérat, Experimental investigations of an oscillating lean premixed ch4/air swirl flame in a gas turbine model combustor, Proceedings of the European Combustion Meeting, 2005.
[42] P. Weigand, W. Meier, X. Duan, M. Aigner, Laser-Based Investigations of Thermoacoustic Instabilities in a Lean Premixed Gas Turbine Model Combustor, J. Eng. Gas Turbines Power 129 (2006) 664–671.
[43] Z. Yin, P. Nau, W. Meier, Responses of combustor surface temperature to flame shape transitions in a turbulent bi-stable swirl flame, Exp. Therm. Fluid Sci. 82 (2017) 50–57.
[44] B. Franzelli, E. Riber, L. Y. Gicquel, T. Poinsot, Large Eddy Simulation of combustion instabilities in a lean partially premixed swirled flame, Combust. Flame 159 (2012) 621–637.
[45] B. Franzelli, E. Riber, B. Cuenot, Impact of the chemical description on a Large Eddy Simulation of a lean partially premixed swirled flame, Comptes Rendus Mécanique 341 (2013) 247–256.
[46] D. Fredrich, W. P. Jones, A. J. Marquis, The stochastic fields method applied to a partially premixed swirl flame with wall heat transfer, Combust. Flame 205 (2019) 446–456.
[47] J. Galpin, A. Naudin, L. Vervisch, C. Angelberger, O. Colin, P. Domingo, Large-eddy simulation of a fuel-lean premixed turbulent swirl-burner, Combust. Flame 155 (2008) 247–266.
[48] B. Fiorina, R. Vicquelin, P. Auzillon, N. Darabiha, O. Gicquel, D. Vey-

nante, A filtered tabulated chemistry model for les of premixed combustion, Combust. Flame 157 (2010) 465–475.
[49] G. Albouze, T. Poinsot, L. Gicquel, Chemical kinetics modeling and les combustion model effects on a perfectly premixed burner, Comptes Rendus Mécanique 337 (2009) 318–328.
[50] J. M. Lourier, M. Stöhr, B. Noll, S. Werner, A. Fiolitakis, Scale Adaptive Simulation of a thermoacoustic instability in a partially premixed lean swirl combustor, Combust. Flame 183 (2017) 343–357.
[51] P. S. Volpiani, T. Schmitt, D. Veynante, Large eddy simulation of a turbulent swirling premixed flame coupling the TFLES model with a dynamic wrinkling formulation, Combust. Flame 180 (2017) 124–135.
[52] D. Fredrich, W. P. Jones, A. J. Marquis, Thermo-acoustic instabilities in the preccinsta combustor investigated using a compressible les-pdf approach, Flow Turbul. Combust. (2020) 1–17.
[53] B. Higgins, M. Q. McQuay, F. Lacas, J. C. Rolon, N. Darabiha, S. Candel, Systematic measurements of OH chemiluminescence for fuel-lean, high-pressure, premixed, laminar flames, Fuel 80 (2001) 67–74.
[54] F. Nicoud, H. B. Toda, O. Cabrit, S. Bose, J. Lee, Using singular values to build a subgrid-scale model for large eddy simulations, Phys. Fluids 23 (2011) 085106.
[55] O. Colin, M. Rudgyard, Development of High-Order Taylor-Galerkin Schemes for LES, J. Comput. Phys. 162 (2000) 338–371.
[56] T. Poinsot, S. Lele, Boundary conditions for direct simulations of compressible viscous flows, J. Comput. Phys. 101 (1992) 104–129.
[57] P. W. Agostinelli, B. Rochette, D. Laera, J. Dombard, B. Cuenot, L. Gicquel, Static mesh adaptation for reliable large eddy simulation of turbulent reacting flows, Phys. Fluids 33 (2021) 035141.
[58] J. P. Legier, T. Poinsot, D. Veynante, Dynamically thickened flame LES model for premixed and non-premixed turbulent combustion, Proc. Summer Program, Cent. Turbul. Res. (2000) 157–168.
[59] F. Charlette, D. Veynante, C. Meneveau, A power-law wrinkling model for LES of premixed turbulent combustion: Part I - non-dynamic formulation and initial tests, Combust. Flame 131 (2002) 159–180.
[60] G. P. Smith, Gri-mech 3.0, http://www. me. berkley. edu/gri_mech/.
[61] M. F. Modest, Radiative heat transfer, Academic press, 2013.
[62] W. L. Grosshandler, RADCAL: A Narrow Band Model for Radiation, NIST Tech. note 1402, 1993.
[63] S. Whitaker, Forced convection heat transfer correlations for flow in pipes, past flat plates, single cylinders, single spheres, and for flow in packed beds and tube bundles, AIChE J. 18 (1972) 361–371.
[64] S. W. Churchill, H. H. Chu, Correlating equations for laminar and turbulent free convection from a vertical plate, Int. J. Heat Mass Transf. 18 (1975) 1323–1329.
[65] F. P. Incropera, A. S. Lavine, T. L. Bergman, D. P. DeWitt, Fundamentals of heat and mass transfer, Wiley, 2007.
[66] L. Rayleigh, The explanation of certain acoustical phenomena, Roy. Inst. Proc. 8 (1878) 536–542.
[67] Y. Huang, V. Yang, Dynamics and stability of lean-premixed swirl-stabilized combustion, Prog Energ Combust 35 (2009) 293–364.
[68] T. Lieuwen, V. Yang (Eds.), Combustion instabilities in gas turbine engines: operational experience, fundamental mechanisms and modeling, Progress in astronautics and aeronautics, American Institute of Aeronautics and Astronautics, Reston, VA, USA, 2005.
[69] L. Selle, F. Nicoud, T. Poinsot, Actual Impedance of Nonreflecting Boundary Conditions: Implications for Computation of Resonators, AIAA J. 42 (2004) 958–964.
[70] G. Daviller, G. Oztarlik, T. Poinsot, A generalized non-reflecting inlet boundary condition for steady and forced compressible flows with injection of vortical and acoustic waves, Comput. Fluids 190 (2019) 503–513.
[71] J. Miles, The reflection of sound due to a change in cross section of a circular tube, The Journal of the Acoustical Society of America 16 (1944) 14–19.
[72] F. Duchaine, A. Corpron, L. Pons, V. Moureau, F. Nicoud, T. Poinsot, International Journal of Heat and Fluid Flow Development and assessment of a coupled strategy for conjugate heat transfer with Large Eddy Simulation : Application to a cooled turbine blade, Int. J. Heat Fluid Flow 30 (2009) 1129–1141.
[73] F. Duchaine, S. Mendez, F. Nicoud, A. Corpron, Conjugate heat transfer with Large Eddy Simulation for gas turbine components, Comptes Rendus Mécanique 337 (2009) 550–561.
[74] F. Duchaine, S. Jauré, D. Poitou, E. Quémerais, G. Staffelbach, T. Morel, L. Gicquel, Analysis of high performance conjugate heat transfer with the OpenPALM coupler, Comput. Sci. Discov. 8 (2015) 15003.
[75] C. Willert, Stereoscopic digital particle image velocimetry for application in wind tunnel flows, Meas. Sci. Technol. 8 (1997) 1465–1479.
[76] F. Nicoud, L. Benoit, C. Sensiau, T. Poinsot, Acoustic modes in combustors with complex impedances and multidimensional active flames, AIAA J. 45 (2007) 426–441.
[77] P. J. Schmid, Dynamic mode decomposition of numerical and experimental data, J. Fluid Mech. 656 (2010) 5–28.
[78] F. Richecoeur, L. Hakim, A. Renaud, L. Zimmer, Dmd algorithms for experimental data processing in combustion, Proc. Summer Program, Cent. Turbul. Res. (2012) 459–468.
[79] L. Magri, M. P. Juniper, J. P. Moeck, Sensitivity of the rayleigh criterion in thermoacoustics, J. Fluid Mech. 882 (2020) 1–11.
[80] E. Lo Schiavo, D. Laera, E. Riber, L. Gicquel, T. Poinsot, On the impact of fuel injection angle in Euler–Lagrange large eddy simulations of swirling spray flames exhibiting thermoacoustic instabilities, Combust. Flame 227 (2021) 359–370.